

Proceedings of the Computational Medical Physics Working Group Workshop I: CMPWG I

Date August 2006

Compiled by
Bernadette L. Kirk
Alice F. Rice

DOCUMENT AVAILABILITY

Reports produced after January 1, 1996, are generally available free via the U.S. Department of Energy (DOE) Information Bridge.

Web site <http://www.osti.gov/bridge>

Reports produced before January 1, 1996, may be purchased by members of the public from the following source.

National Technical Information Service
5285 Port Royal Road
Springfield, VA 22161
Telephone 703-605-6000 (1-800-553-6847)
TDD 703-487-4639
Fax 703-605-6900
E-mail info@ntis.fedworld.gov
Web site <http://www.ntis.gov/support/ordernowabout.htm>

Reports are available to DOE employees, DOE contractors, Energy Technology Data Exchange (ETDE) representatives, and International Nuclear Information System (INIS) representatives from the following source.

Office of Scientific and Technical Information
P.O. Box 62
Oak Ridge, TN 37831
Telephone 865-576-8401
Fax 865-576-5728
E-mail reports@adonis.osti.gov
Web site <http://www.osti.gov/contact.html>

This report was prepared as an account of work sponsored by an agency of the United States Government. Neither the United States government nor any agency thereof, nor any of their employees, makes any warranty, express or implied, or assumes any legal liability or responsibility for the accuracy, completeness, or usefulness of any information, apparatus, product, or process disclosed, or represents that its use would not infringe privately owned rights. Reference herein to any specific commercial product, process, or service by trade name, trademark, manufacturer, or otherwise, does not necessarily constitute or imply its endorsement, recommendation, or favoring by the United States Government or any agency thereof. The views and opinions of authors expressed herein do not necessarily state or reflect those of the United States Government or any agency thereof.

**PROCEEDINGS OF THE COMPUTATIONAL MEDICAL
PHYSICS WORKING GROUP WORKSHOP I: CMPWG I**

**Compiled by
Bernadette L. Kirk
Alice F. Rice**

Date Published: August 2006

Prepared by
OAK RIDGE NATIONAL LABORATORY
P.O. Box 2008
Oak Ridge, Tennessee 37831-6285
managed by
UT-Battelle, LLC
for the
U.S. DEPARTMENT OF ENERGY
under contract DE-AC05-00OR22725

Contents

PREFACE	v
Participants	vii
Brachytherapy, <i>Mark Rivard</i> , New England Medical Center, Tufts University	1
Computational Benchmarks for Medical Physics, <i>Robert Jeraj</i> ¹ , <i>Michael E. Kowalok</i> ² , and <i>Benny Titz</i> ¹ (¹ Department of Medical Physics, University of Wisconsin, Madison, WI; ² Virginia Commonwealth University, Richmond, VA.....	5
Proton Radiation Cancer Therapy, <i>Wayne Newhauser</i> , M.D. Anderson Cancer Center.....	13
Overview of Deterministic Radiation Transport Methods, <i>M. L. Williams</i> and <i>R. A. Lillie</i> , Oak Ridge National Laboratory.....	15
Doors Radiation Transport Code System, <i>R. A. Lillie</i> , Oak Ridge National Laboratory	27
MCNP / MCNPX Overview from a Medical Physics Perspective, <i>Tim Goorley</i> , MCNP Team, X-3, Los Alamos National Laboratory	39
PENTRAN Code System, <i>Glenn Sjoden</i> and <i>Ali Haghghat</i> , University of Florida.....	41
Coarse Mesh Radiation Transport Code COMET: Radiation Therapy Application, <i>Farzad Rahnema</i> , <i>Megan Satterfield</i> and <i>Dingkang Zhang</i> , Nuclear and Radiological Engineering and Medical Physics Programs, George W. Woodruff School, Georgia Institute of Technology.....	45
MINERVA: A Multimodality Plugin-Based Radiation Therapy Treatment Planning System, <i>Dave Nigg</i> , Idaho National Laboratory.....	47
TRANSMED: Deterministic Photon Transport for External Beam Therapy, <i>Erno Sajo</i> (Louisiana State University, Department of Physics) and <i>Mark L. Williams</i> (Oak Ridge National Laboratory).....	51
Introduction to A ³ MCNP – Automated Adjoint Accelerated MCNP, <i>A. Haghghat</i> , Department of Nuclear and Radiological Engineering, University of Florida	59
A Revised Stylized Phantom and Voxelized Model of the Extrathoracic and Thoracic Regions for use in Nuclear Medicine Internal Dosimetry, <i>Eduardo B. Farfán</i> , Idaho State University	63

PREFACE

The first workshop of the Computational Medical Physics Working Group (CMPWG) of the American Nuclear Society was held on October 26, 2005. CMPWG was formed in November 2004 within the American Nuclear Society (ANS) and is jointly hosted by three ANS divisions—Mathematics and Computations, Biology and Medicine, Radiation Protection and Shielding. CMPWG consists of individuals from the *American Nuclear Society (ANS)*, *American Association of Physicists in Medicine (AAPM)*, *Society of Nuclear Medicine (SNM)*, *Health Physics Society (HPS)* among others. It is an international group dedicated to the validation and advancement of computational tools in medical and health physics applications. The CMPWG website is <http://cmpwg.ans.org>.

The workshop was held to address several key areas:

- Identify the medical physics problems and experiments for computational benchmarks
- Identify the software tools, their applications, strengths and weaknesses
- Identify applications suitable for parallel computing
- Identify the roadmap for benchmarking activities.

Discussions centered on the need for experimental data, the importance of both Monte Carlo and deterministic methods, and the need to evaluate current nuclear data for medical physics. These activities are aimed at improving dose predictions for radiation therapy and other medical activities that utilize ionizing radiation.

The ensuing sections describe representative topics that were discussed at the workshop.

NOTE: The papers included in this report are presented as provided by the authors. They are reproduced here without alteration to the content. Any changes that have been made are strictly cosmetic. The viewgraphs for all the presentations may be found at <http://cmpwg.ans.org/workshop.html>.

Participants

Cassiano De Oliveira, Georgia Tech
Eduardo Farfan, Idaho State
Tim Goorley, Los Alamos National Laboratory
Ali Haghighat, University of Florida
Robert Jeraj, University of Wisconsin
Wayne Newhauser, M.D. Anderson Cancer Center
Trent Nichols, UT Medical Center
Dave Nigg, Idaho National Laboratory
Farzad Rahnema, Georgia Tech
Mark Rivard, Tufts University New England Medical Center
Erno Sajo, Louisiana State University
Glenn Sjoden, University of Florida

ORNL Participants

Hatice Akkurt
Kevin Clarno
Mike Dunn
Dan Ilas
Germina Ilas
Bernadette Kirk
Luiz Leal
Dick Lillie
Saed Mirzadeh
Douglas Peplow
John Wagner
Mark Williams

BRACHYTHERAPY

Mark Rivard
New England Medical Center
Tufts University

Brachytherapy is a form of radiation therapy in which sealed radiation sources are in close contact to the human body, or even inserted within the body [Nath et al, 1995]. Brachytherapy was conceived in 1903, is most often used for the treatment of cancer, and approximately 160,000 patients per year receive this type of treatment. The first half of the 20th century primarily used ²²⁶Ra and ²²²Rn for brachytherapy; these sources emit photons with energies exceeding 1 MeV. Following construction of nuclear reactors and improvements in radiochemistry, a wide assortment of radionuclides became available. Major advances in the later half of the 20th century were to use sources with photon emissions of much lower energy so that hospital staff were not unduly irradiated while caring for the sick. ¹²⁵I and ¹⁰³Pd are low-energy photon-emitting sources with average energies < 0.03 MeV, and half-lives of 59 and 17 days, respectively [Rivard et al, 2004]. Due to their short half-lives and “soft” emissions, they are ideal candidates for permanent implantation for some cancer types. Because the implantation process is physically invasive, the sealed sources may be handled roughly during the surgical process [Yu et al, 1999]. Therefore, they are often encapsulated in a strong yet ductile material such as Ti. This aspect is important and will be discussed shortly.

For radiological measurements in medicine, air ionization chambers are often used since they are easy to use, exhibit tremendous reproducibility and signal-to-noise characteristics, and demonstrate constancy when accounting for temperature and pressure corrections. The National Institute of Standards and Technology (NIST) is the primary standards laboratory for the U.S., and calibrates source strength for medical purposes using air kerma strength. For low-energy photon-emitting brachytherapy sources such as ¹²⁵I and ¹⁰³Pd, the NIST Wide Angle Free Air Chamber (WAFAC) in Fig. 1 is used [Seltzer et al, 2003]. This large ionization chamber directly measures the kinetic energy released in air from low-energy photon-emitting brachytherapy sources positioned at a calibration point, with total k=2 uncertainties < 3%. The NIST WAFAC measures photons over a large energy range, including the Ti K-edge characteristic x-rays made by radioactive ¹²⁵I and ¹⁰³Pd photon emissions. These K-edge photons have an average energy of ~ 4.5 keV, with a mean path length of ~ 20 cm in air and 0.2 mm in water. Therefore, the photons could cause substantial signal in the WAFAC yet will negligibly contribute dose within the patient at clinically relevant distance which are often > 5 cm [Kubo, 1985]. To ameliorate Ti K-edge x-ray contamination, an aluminum filter is used to preferentially attenuate the 4.5 keV x-rays while transmitting the higher energy photons.

The NIST WAFAC was designed at a time when there were in total three ¹²⁵I and ¹⁰³Pd sources available. Currently, over 30 different source models have been measured with the WAFAC, and additional radionuclides such as ¹³¹Cs and ¹⁷⁰Tm are being developed. As all these brachytherapy source models will have different photon spectra, it is of interest to simulate the NIST WAFAC to better understand the dependence of various corrections on photon energy and subsequently for these new sources.

Due to the complex geometry of the NIST WAFAC, the most accurate simulations will provide 3D characterization, and account for both photon and electron transport. Furthermore, simulation accuracy may be further enhanced by accounting for the electric

fields and resultant collecting volume. Radiation transport codes which may be suitable for these purposes include MCNP, PENELOPE, and EGS4, and would certainly benefit from parallel computing due to the complex physics simulations and complicated source:NIST WAFAC geometries. These calculations should be complemented through use of reference sources with customized dimensions and capsule material to evaluate the simulation data and rigor of the NIST WAFAC correction methodology. Knowledge gained would:

- a) improve accuracy and validate correction methodologies used at NIST,
- b) could result in modifications to the NIST WAFAC, fabrication of a more generalized detector, or even entirely new measurement methodologies, and
- c) could be used to improve the accuracy of low-energy (< 10 keV) photon cross-sections and reliant physics in the transport codes.

References

1. R. Nath, L. L. Anderson, G. Luxton, K. A. Weaver, J. F. Williamson, and A. S. Meigooni, "Dosimetry of interstitial brachytherapy sources: Recommendations of the AAPM Radiation Therapy Committee Task Group No. 43," *Med. Phys.* 22, 209–234 (1995).
2. M. J. Rivard, B. M. Coursey, L. A. DeWerd, W. F. Hanson, M. S. Huq, G. S. Ibbott, M. G. Mitch, R. Nath, and J. F. Williamson, "Update of AAPM Task Group No. 43 Report: A revised AAPM protocol for brachytherapy dose calculations," *Med. Phys.* 31, 633-674 (2004).
3. Y. Yu, L. L. Anderson, Z. Li, D. E. Mellenberg, R. Nath, M. C. Schell, F. M. Waterman, A. Wu, and J. C. Blasko, "Permanent prostate seed implant brachytherapy: Report of the American Association of Physicists in Medicine Task Group No. 64," *Med. Phys.* 26, 2054-2076 (1999).
4. S. M. Seltzer, P. J. Lamperti, R. Loevinger, M. G. Mitch, J. T. Weaver, and B. M. Coursey, "New national air-kerma-strength standards for ^{125}I and ^{103}Pd brachytherapy seeds," *J. Res. Natl. Inst. Stand. Technol.* 108, 337-358 (2003).
5. H. Kubo, "Exposure contribution from Ti K x rays produced in the titanium capsule of the clinical ^{125}I seed," *Med. Phys.* 12, 215–220 (1985).

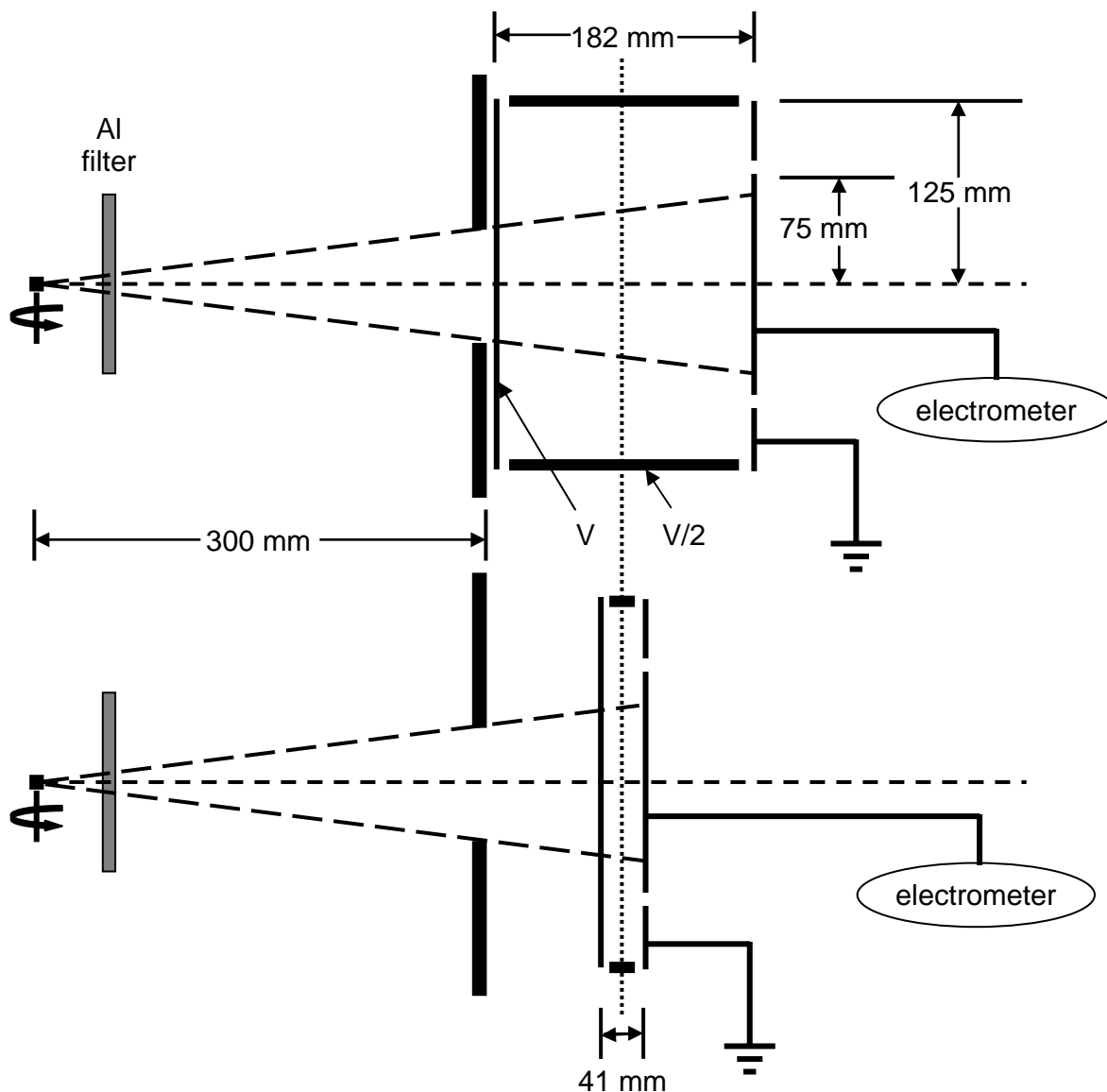


Fig. 1. The WAFAC measurement scheme, involving the subtraction of the results of a second measurement using the small chamber length (lower diagram) in order to remove any possible effects due to the presence of the front and back aluminized-mylar electrodes. The middle electrode lengths shown are for the original WAFAC. The seed is rotated during measurement, resulting in an effective averaging of air kerma rate with respect to azimuth angle, correcting for anisotropy in the transverse-plane. Perturbation by the aluminized-mylar electrodes or fringing of the electric field are removed by subtracting the charge measured for a small chamber length (lower diagram) from that for the large chamber length (upper diagram). This approach renders the WAFAC measurements to be those of a free-air chamber, and measured charges are associated with slowing down of electrons arising from photon collisions in an effective volume equal to the aperture area times the difference in the chamber lengths.

COMPUTATIONAL BENCHMARKS FOR MEDICAL PHYSICS

Robert Jeraj¹, Michael E. Kowalok², Benny Titz¹

¹Department of Medical Physics, University of Wisconsin, Madison, WI

²Virginia Commonwealth University, Richmond, VA

Modern radiation therapy is enabled by computer-controlled technologies and computational tools that allow for the accurate localization and diagnosis of disease (imaging) and the design, simulation, delivery, and verification of radiation treatments. Recent developments that fuse information from multiple imaging modalities such as CT and PET have enabled “image-guided” radiotherapy techniques, and have placed the role of computer simulation at the very center of radiation therapy. With this increasing reliance on computational tools, an increasing need is evident for the benchmarking and quality assurance of the computer models and codes that enable accurate simulations for the radiotherapy process.

In this regard, a computational benchmarking initiative is proposed, with the goal of applying established nuclear engineering benchmarking techniques to the radiation transport and dosimetry tools created for medical applications. Computer code benchmarking is a recognized necessity for building robust models and confidence in the reliability of simulated results – especially for applications where physical measurements are not possible for either physical or ethical reasons. In addition, rigorous benchmarking can inform and improve theoretical considerations in radiation dosimetry for medical applications.

The proposed computational benchmarking initiative is fourfold:

- 1) Development of rigorous benchmarking methods for medical physics applications;
- 2) Compilation and review of existing benchmarks with medical applications;
- 3) Design of new benchmarks;
- 4) Implementation of the benchmarking initiative in a multi-institutional, collaborative manner.

A brief summary of each of these components follows.

1. Development of rigorous benchmarking procedures

Established methods for code benchmarking will be adapted and applied to problems in medical physics. Rigorous methods will include a detailed description of the design and method of the benchmark and a detailed description of the uncertainties in relevant data and techniques. The benchmarking procedures for computational benchmarks in medical physics will be developed applying experiences from similar activities in other fields. The following format will be required from the benchmarks, except for theoretical benchmarks, where the items 1 and 2 (pertaining to the experiments) will be omitted.

1. Detailed description of the benchmark
 - a. Overview of the experiment
 - b. Experimental configuration
 - c. Description of material data
 - d. Supplemental experimental measurements
2. Evaluation of experimental data
 - a. Experimental uncertainties
 - b. Material uncertainties

3. Benchmark specifications
 - a. Description of the model
 - b. Dimensions
 - c. Material data
 - d. Environmental data
 - e. Experimental and benchmark-model values
4. Results of sample calculations
 - a. Computer code inputs

2. Compilation of existing benchmarks

Literature has to be reviewed for existing benchmarks, with special emphasis on experimentally supported benchmarks. A preliminary review is given in the Appendix A. The literature has to be thoroughly reviewed for the benchmark quality experiments as well as theoretical benchmarks used for code comparisons. If experiments were considered interesting, but not performed rigorously enough, they will be repeated to bring them to the benchmark quality level. Some theoretical-only benchmarks will be supplemented with experiments.

The benchmarks will be classified according to their medical physics applications; some benchmarks will be applicable to more than one of the groups.

- *Radiation therapy (RT)*
- *Imaging (IM)*
- *Nuclear medicine (NM)*
- *Health physics (HP)*

Some examples: dose distribution on a heterogeneous phantom (RT), CT density phantom (IM), internal dosimetry (NM), MIRD phantoms (HP), dose distributions on the phantoms acquired with MVCT (IM-RT), photo-nuclear production during radiation therapy (RT-HP)

The benchmarks will also be classified in accordance to their nature; some will be applicable to more than one:

- *Theoretical benchmarks (THE)*: testing consistency of the codes
- *Clinical benchmarks (CLI)*: testing clinical – real world – problems
- *Experimental benchmarks (EXP)*: (testing basic input parameters in the codes like cross sections)

Some examples: pencil beam voxel calculation (THE), electron beam backscattering (CLI), thick-target bremsstrahlung production measurements (EXP), heterogeneous phantom dose calculations (THE), if supported by experiments (THE-EXP)

3. Design of new benchmarks

The new benchmark efforts will be focused on designing improved and novel benchmarks in the “conventional” benchmarking areas like basic code testing and clinical experiments. However, refinement of existing benchmarks by performing high precision experiments may also be suggested. Emphasis will be on designing benchmarks that can be verified by physical measurements. The “conventional benchmarks” will be designed in the following areas:

- *Testing the consistency of simulations across different codes* (e.g., modeling of electron transport in optically thin regions, modeling in highly heterogeneous materials, testing cross sections over specified range of energy values)
- *Testing the transport parameters of codes* (e.g., pencil beam calculations in different materials, bremsstrahlung differential cross sections, electron backscattering calculations, ionization chamber measurements, detector simulations)

- *Benchmarks relevant to commonly occurring clinical issues* (e.g., external beam radiation therapy, brachytherapy, internal dosimetry, shielding problems)
- *Imaging benchmarks* (e.g., multi-modality imaging techniques such as PET-CT, where the goal will be to generate quantitative as well as qualitative information, CT (including kilovoltage, megavoltage, and cone-beam applications), PET, MRI, and ultrasound)

In regards to verification of computer codes, comparisons will be made with as many codes as possible and with at least one code common to every benchmark. Codes will be collected into a library, and a database of material specifications, cross-sections, and input files will be established.

4. Implementation of benchmarks

The scope of the benchmarking initiative will be multi-institutional and international. While all of the computational benchmarks will be modeled with at least one of the code (typically MCNP(X) or EGSnrc), they will become the most valuable when as many as possible codes are tested on them. It is expected that this activity will be performed within the general (medical) physics community, stimulating code intercomparison and code improvements. A significant national and international effort has been initiated to perform such a task. Furthermore, agreements have been achieved with some of the main code developers that input code verification will be performed to achieve the highest fidelity of the results. It is planned that a depository of the code inputs will be kept on the tested benchmarks to allow further inter-code comparisons.

Appendix A – Review of the literature for potential Monte Carlo benchmark candidates

	<i>Author(s)</i>	<i>Reference</i>	<i>Title</i>	<i>MC-code(s)</i>	<i>Subject matter</i>	<i>Classif.</i>
1	Bogner, Scherer et al.	Strahlenther. Onkol. 2004; 180:3405-350	Verification of IMRT: Techniques and Problems	XVMC/VEF	Investigation of diff. radiographic films and dose probes for their suitability	THE+EXP
2	Bohm et al.	Med. Phys. 30(4), April 2003	Brachytherapy dosimetry of ¹²⁵ I and ¹⁰³ Pd sources using an updated cross section library for the MCNP transport code	MCNP/MCNPX +improv. cr. sec. lib.	MC benchm. of brachytherapy single source character. with new cr. sec. lib.	CLI+THE
3	Borg, Kawrakow, Rogers, Seuntj.	Conf. Proc. of 22nd EMBS Jul. 23-28 2000	Experimental verification of EGSnrc MC calculated ion chamber response in low energy photon beams	EGSnrc	Experim. verification - comparison of calc. & meas. response of ionization chamber	THE+EXP
4	Carrasco et al.	Med. Phys. 31(10), October 2004	Comparison of dose calc. algorithms in phantoms with lung equivalent heterogeneities under conditions of lat. electronic disequilib.	PENELOPE	PDD benchmark meas. with lung phantom TLDs, ion chamber, MC- & TPS-simulations	THE+EXP
5	Carrier et al.	Med. Phys. 31(3), March 2004	Validation of GEANT4, an object-oriented MC toolkit, for simulations in medical physics	GEANT4 comp. to MCNP, EGS, EGSnrc	Comp. of GEANT4 with other codes and simulation data of multilayer phantom	THE
6	Chetty, Bielajew et al.	Phys. Med. Biol. 47(2002) 1837-51	Exp. Validation of the DPM MC code using minimally scattered electron beams in heterogeneous media	DPM + MCNP4B modelling	(Elec.) Benchm. against meas. PDDs & ion chamber meas. in homo- & heterog. media	EXP
7	Chetty, Bielajew et al.	Med. Phys. 30(4), April 2003	Photon beam relative dose validation of the DPM MC code in lung-equivalent media	DPM + BEAM modelling	(Phot.) Validation at 6 and 15MV in heterogeneous media (lung phantom)	EXP
8	Chibani & Li	Med. Phys. 29(5), May 2002	MC dose calculations in homogeneous media and at interfaces: A comparison between GEPTS, EGSnrc and measurements	GEPTS comp. to EGSnrc, MCNP	Comp. with other codes, simul. & meas. in homo- & heterog. media / at interfaces	THE+EXP
9	Chibani & Li	Med. Phys. 30(1), January 2003	IVBTMC, a Monte carlo dose calculation tool for intravascular brachytherapy	IVBTMC (based on EGSnrc)	Verification against other codes (EGSnrc & MCNP) and exp. using radio-chromic films	THE+EXP
10	Chow et al.	Med. Phys. 30(10), October 2003	Comparison of dose calculation algorithms with Monte Carlo methods for photon arcs	MC, PBeamKernel, CCC, EGS/DOSXYZ	calc. of 3D dose distrib. In different phantoms; TPS and IC measurements	THE+EXP
11	Cygler, Ding et al.	Med. Phys. 31(1), January 2004	Evaluation of the first commercial MC dose calculation engine for electron beam treatment planning	VMC++ (Kawrakow)	Calc. vs. meas. data in homo- & heterogen. phantoms at diff. SSDs and gantry angles	THE+EXP
12	Ding	Med. Phys. 29(11), November 2002	Dose discrepancies between Monte Carlo calculations and measurements in the buildup region for a high-energy photon beam	EGS4/DOSXYZ EGSnrc/DOSRZnrc	Calculations vs. IC-measurements of DD	THE+EXP
13	Doucet, Olivares et al.	Phys. Med. Biol. 48(2003) 2339-2354	Comparison of measured and MC calc. dose distributions in inhomogeneous phantoms in clinical electron beams	XVMC & EGSnrc	Irradiation with 9 and 15 MeV beams, TLD measurements in solid water phantoms	THE+EXP
14	Faddegon & Rogers	Nuc.Instr.Meth.Phys. A327 (1993) 556-565	Comparison of thick-target bremsstrahlung calculations by EGS4/Presta and ITS 2.1	EGS/Presta ITS Version 2.1	Calc. of spectral distr. without meas. in 10-20 MeV beams of Be, Al and Pb targets	THE
15	Faddegon, Ross & Rogers	Med. Phys. 18(4), Jul./Aug. 1991	Angular distribution of bremsstrahlung from 15MeV electrons incident on thick targets of Be, Al and Pb	EGS4	Measurements vs. calculation of bremsstrahlung spectra at certain angles	THE+EXP

	<i>Author(s)</i>	<i>Reference</i>	<i>Title</i>	<i>MC-code(s)</i>	<i>Subject matter</i>	<i>Classif.</i>
16	Flampouri, Verhaegen et al.	Phys. Med. Biol. 47(2002) 3331-49	Optimization of accelerator target and detector for portal imaging using MC simulation and experiment	EGS4/BEAM	Sim. & experim. of image contrast to max. image quality - test diff. hardw. combos	THE+EXP
17	Fragoso, Nahum, Verh. et al.	Med. Phys. 30(6), June 2003	Incorporation of a combinatorial geometry package and improved scoring capabilities in the EGSnrc MC Code system	GenUC (generic EGSnrc user code)	Incorporation/Implementation of GenUC and benchmarking against EGSnrc, DOSRZnrc	THE
18	Heath, Seuntjens, Sh.-Bagheri	Med. Phys. 31(10), October 2004	Dosimetric evaluation of the clinical implementation of the first commercial IMRT TPS at 6MV	PEREGRINE (TPS) comp. to EGSnrc	Dosimetrically eval. of PEREGRINE - meas. in diff. phantoms vs. EGSnrc calculations	THE+EXP
19	Hirayama	IEEE Transact. Nuc. 40(4) August 1993	MC-Simulations with EGS4/Presta for an EM Sampling Calorimeter	EGS4, EGS4/Estepa EGS4/Presta	Sim. of an e/m sampling calorimeter using a thin silicon detector vs. experim. Data	THE+EXP
20	Insoo Jun	IEEE Transact. Nuc. 50(5) October 2003	Benchmark Study for Energy Deposition by energetic electrons in thick elemental slabs: MC results and experiment	MCNP4c TIGER3.0	Sim. vs. meas. of energy deposition profiles of electr. impinging on slabs	THE+EXP
21	Jeraj et al.	Phys. Med. Biol. 44(1999) 705-717	Comparison between MCNP, EGS4 and experiment for clinical electron beams	MCNP & EGS4	Comparison of EGS4, MCNP(4B & ITS) and Experiment	THE+EXP
22	Kawrakow, Fippel, Friedrich	Med. Phys. 23(4), April 1996	3D electron dose calculation using a voxel based MC algorithm (VMC)	VMC comp. to EGS4 and MDAH (Hogstr.)	Implementation of VMC and comparison (only calc.) to EGS4 and MDAH	THE
23	Keall, Siebers, Jeraj & Mohan	Medical Dosimetry 28(2), summer 2003	Radiotherapy dose calculations in the presence of hip prostheses	EGS4 DOSXYZ+BEAM	Comparison of MC, superposition, pencil beam and no-heterogeneity corr. algor.	THE+CLI
24	Lauterbach et al.	Nuc.Instr.Meth.Phys. B152 (1999) 212-220	Energy deposition of electrons in low-, medium- and high-Z material: Comparison of the MC transport code EGS4 with experiment	EGS4 + Presta2 prototype	Simulation vs. meas. with ion. chamber... at 4, 10, 20 MeV and diff. materials	THE+EXP
25	Lewis et al.	Phys. Med. Biol. 45(2000) 1755-1764	Use of MC computation in benchmarking radiotherapy treatment planning system algorithms	TPS comparison using MCNP4B	Diff. TPS + abs. dose meas. in a heterogen. medium - comp. to film dosimetry	THE+EXP
26	Love, Lewis et al.	Phys. Med. Biol. 43(1998) 1351-1357	Comp. of EGS4 and MCNP MC codes when calculating radiotherapy depth doses	EGS4 & MCNP	calculated DD in water for monoenergetic photons, comp. with published data	THE
27	Luxton	Med. Phys. 21(5), May 1994	Comparison of radiation dosimetry in water and in solid phantom materials for (...) brachytherapy sources: EGS4 MC study	EGS4	Calc. vs. meas. of dose rate to water within a water substitute solid phantom	THE+EXP
28	Ma & Nahum	Phys. Med. Biol. 40(1995) 45-62	Calculations of ion chamber displacement effects corrections for medium-energy x-ray dosimetry	EGS4	Simulation of coupled photon-electron transport at tube potent. betw. 100-300kV	THE
29	Ma & Nahum	Phys. Med. Biol. 38(1993) 93-114	Dose conversion and wall correction factors for Fricke dosimetry in high-energy photon beams: analytical model & MC calculations	EGS4 comp. to correlated sampling	MC calculation of wall-correction factors and comparison to other authors	THE
30	Ma et al.	Phys. Med. Biol. 45(2000) 2483-2495	MC verification of IMRT dose distributions from a commercial treatment planning optimization system	EGS4/BEAM EGS4/DOSXYZ	Verification of the IMRT dose distribution meas. in homogeneous water phantom	THE+EXP
31	Mainegra, Capote	Proc. of the 2nd int. workshop on EGS	Dosimetric characterisation of low energy brachytherapy sources: an EGS4 MC study	EGS4	Calc. vs. meas. results of two dim. dose rate distrib. In water, calc. of air kerma	THE+EXP

	<i>Author(s)</i>	<i>Reference</i>	<i>Title</i>	<i>MC-code(s)</i>	<i>Subject matter</i>	<i>Classif.</i>
32	Martens et al.	Med. Phys. 29(7), July 2002	Underdosage of the upper-airway mucosa for small fields as used in IMRT: (...)	EGSnrcBEAM, PB, CCC(He.), CCC(Pin.)	Comparison of MC, PB and CCC-codes for head and neck tumors	THE+EXP+CLI
33	Marziani et al.	Proc. of the MC 2000 Conference	MC simulation of mammography x-ray units: a comparison between different electron extension of the EGS4 code system	enhanced versions of EGS4	simulations of tube response at 26-30kVp	THE
34	Mercier et al.	Med. Phys. 27(12), December 2000	Modification and benchmarking of MCNP for low-energy tungsten spectra	MCNP	modif. code till 150keV range of backsc. factors, prim. and sc. photon transp.	THE
35	Mobit, Nahum & Mayles	Phys. Med. Biol. 42(1997) 1319-1334	An EGS4 MC examination of general cavity theory	EGS4	MC sim. and meas. to examine gen. cavity theory for different TLD cav. materials	THE+EXP
36	Mobit, Nahum & Mayles	Phys. Med. Biol. 41(1996) 387-398	The quality dependence of LiF TLD in megavoltage photon beams: MC simulations and experiments	EGS4	Exp. studies against ion chamber measurements	THE+EXP
37	Nilsson, Montelius & Andreo	Med. Phys. 19(6), Nov/Dec 1992	A study of interface effects in ⁶⁰ Co beams using a thin-walled parallel plate ionization chamber	EGS4+Presta+DOSRZ 4.0	Calc. vs. meas. data with diff. backscatter materials of different atomic numbers	THE+EXP
38	Nilsson, Montelius & Andreo	Phys. Med. Biol. 41(1996) 609-623	Wall effects in plane-parallel ionization chambers	EGS4 DOSRZ	Calc. vs. Meas., determ. of wall perturb. with exchangeable front and back walls	THE+EXP
39	Nirayama, Hirayama et al.	Phys. Med. Biol. 46(2001) 717-728	Dose measurements in inhomogeneous bone/tissue and lung/tissue phantoms for angiography using synchrotron radiation	EGS4	absorbed dose measurements with thin TLDs & comp. to calc. data	THE+EXP
40	Paelinck, Reynaert et al.	Phys. Med. Biol. 48(2003) 1895-1905	The value of radiochromic film dosimetry around air cavities: experimental results and Monte Carlo simulations	BEAMnrc, EGSnrc DOSXYZnrc	particular focus on the perturb. of the dose distrib. by the film parallel to the beam axis	THE+EXP
41	Reniers, Verhaegen, Vyncker	Phys. Med. Biol. 49(2004) 1569-1582	The radial dose function of low-energy brachytherapy seeds in diff. solid phantoms: comparison between calc. (...) and meas.	EGSnrc & MCNP4C	Brachyth. seeds: calc. vs. meas. of radial dose function with 2 different codes	THE+EXP+CLI
42	Reynaert & Haefeli	Med. Phys. 28(9), September 2001	Self-absorption correction for ³² P, ¹⁹⁸ Au and ¹⁸⁸ Re stents: Dose point kernel calculations versus Monte Carlo	DosePointKernel to EGS4 & MCNP	Calc. of dose distribution around kernels in comparison to MC calculated results	THE
43	Reynaert et al.	Phys. Med. Biol. 49(2004) N235-N241	MCDE: a new MC dose engine for IMRT	MCDE (based on BEAMnrc/DOSXYZ)	Comparison of clinical example with the collapsed cone convolution calculation	THE
44	Reynaert et al.	Med. Phys. 29(10), October 2002	Parameter dependence of the MCNP electron transport in determining dose distributions	MCNP	detailed study of the dep. of electron transport and energy binning on dose distr.	THE
45	Rogers & Kawrakow	NRCC Report PIRS-703	QA tests of the EGSnrc system and comparison with EGS4	EGSnrc / EGS4	x x x	X
46	Sanchez-Doblado et al	Phys. Med. Biol. 48(2003) 2081-2099	Ionization chamber dosimetry of small photon fields: a MC study on stopping-power ratios for radiosurgery and IMRT beams	EGS4/BEAM	Calculation vs. film dosimetry, diodes, small ionization chamber	THE+EXP
47	Schaart et al.	Phys. Med. Biol. 47(2002) 1459-1484	A comparison of MCNP4C electron transport with ITS3.0 and experiment at incident energies between 100keV and 20MeV: (...)	MCNP4C comp. to ITS 3.0	cell boundaries vs. segments and comp. to previously publ. dose measurements	THE+EXP

	<i>Author(s)</i>	<i>Reference</i>	<i>Title</i>	<i>MC-code(s)</i>	<i>Subject matter</i>	<i>Classif.</i>
48	Scherer, Bogner et al.	Z. Med. Phys. 8(1998) 87-95	MC-Methoden zur direkten Berechnung von 3D-Dosisverteilungen bei Photonenfeldern in der Strahlentherapie	CHILD MC-Code comp. to EGS4	Calc. vs. meas.: Monaco Matrix, EGS4 and dose meas. in water	THE+EXP
49	Sempau J et al.	Phys. Med. Biol. 49(2004) 4427-4444	Electron beam quality correction factors for plane-parallel ionization chambers: MC calculations using the PENELOPE system	PENELOPE	sim. of three different ion chambers for 4-20 MeV and comp. with dosimetry protocol	THE
50	Sempau J et al.	Nuc. Instr. and Meth. in Physics Research	Experimental benchmarks of the MC code PENELOPE	PENELOPE	Comprehensive comparison of simulation results with exp. data from literature	THE+EXP
51	Sheikh-Bagheri, Rogers et al.	Med. Phys. 27(10), October 2000	Comparison of measured and MC calculated dose distributions from the NRC linac	EGS4/BEAM DOSXYZ+SPRXYZ	Calc. vs. meas. of dose distribution in water for 10 and 20 MV photons	THE+EXP
52	Siantar, Bielaj., Faddeg. et al.	Med. Phys. 28(7), July 2001	Description and dosimetric verification of the PEREGRINE MC dose calculation system for photon beams incident on a water phantom	PEREGRINE (TPS) +BEAM modelling	Calc. vs. meas. in water phantom: open, wedged- & MLC-modified fields	THE+EXP
53	Siebers J.V.	Phys. Med. Biol. 47(2002) 3225-3249	A method for photon beam MC multileaf collimator particle transport	MCV MC?	Comparison of 6MV and 18MV photon beams models with measurement	THE+EXP
54	Siebers J.V.	Phys. Med. Biol. 44(1999) 3009-3026	Comparison of EGS4 and MCNP4b MC codes for generation of photon phase space distribution for a Varian 2100C	MCNP4B & EGS4	Comparison of PSDs for 6 and 18MV phot. to determine different in patient dose	THE
55	Siebers, Keall, Mohan et al.	Med. Phys. 31(7), July 2004	MC computation of dosimetric amorphous silicon electronic portal images	EGS4 based (?)	Quantitative comparison betw. meas. and computed portal images	THE+EXP
56	Siebers, Lauterb., Mohan et al.	Med. Phys. 29(2), February 2002	Reducing dose calculation time for accurate iterative IMRT planning	ratio method & correction method	Validation of both methods through TP development and comparison	THE+CLI
57	Stary V.	Proc. of the MC 2000 Conference	Comparison of MC simulation and measurement of electron reflection from solids	PWADIR	Comp. with experimental values meas. at 0.4-2.0 and 0.1-1.5 keV	THE+EXP
58	Trindade, Rodrigues et al.	Proc. of the MC 2000 Conference	MC simulation of electron beams for radiotherapy - EGS4, MCNP4b and GEANT3 intercomparison	EGS4, MCNP4b GEANT3	Intercomp. of electron energy spectra, anglul. and spatial distrib. in water phantom	THE+EXP
59	Van der Walle, Reynaert et al.	Phys. Med. Biol. 48(2003) 371-385	MC model of the Elekta Sliplus accelerator: Validation of a new MLC component module in BEAM for a 6MV beam	BEAM+MLCE BEAM+MLCQ	Implementation of a new component module in the BEAM programm: meas. and simul.	THE+EXP +CLI?
60	Verhaegen & Seuntj. (Comm.)	Med. Phys. Biol. 48(2003) L43-L48	Comments on 'Ionization chamber dosimetry of small photon fields: a MC study on stopping-power ratios for radiosurg. and IMRT beams'	#	Comments on Sanchez-Doblado 2003	X
61	Verhaegen et al.	Med. Phys. Biol. 45(2000), 3159-3170	Backscatter towards the monitor ion chamber in high-energy photon and electron beams: charge integration versus MC simulation	EGS4/BEAM	Calc. vs. meas. of the contribution of backscattered part. to the monitor IC	THE+EXP
62	Verhaegen F.	Phys. Med. Biol. 47(2002) 1691-1705	Evaluation of the EGSnrc MC code for interface dosimetry near high-Z media exposed to kilovolt and 60Co photons	EGSnrc	Investig. of dose perturb. of high-Z heterogen. in kV and 60Co beams	THE+EXP
63	Verhaegen F.	Phys. Med. Biol. 48(2002) 687-705	Interface perturbation effects in high-energy electron beams	EGSnrc	study of dose & fluence perturb. For 4-18MeV beams at backsc. interf. of diff mat.	THE+EXP

	<i>Author(s)</i>	<i>Reference</i>	<i>Title</i>	<i>MC-code(s)</i>	<i>Subject matter</i>	<i>Classif.</i>
64	Verhaegen, Nahum et al.	Med. Phys. 28(6), June 2001	Monte Carlo calculation of output factors for circular, rectangular and square fields of electron accelerators (6-20 MeV)	EGS4/BEAM	Calc. vs. meas. of 6-20MeV beams, comp. of lat. and DD distrib. + Markus chamber	THE+EXP
65	Verhaegen, Nahum et al.	Phys. Med. Biol. 44(1999) 1767-1789	MC modelling of radiotherapy kV x-ray units	EGS4/BEAM comp. to MCNP	Study of photon spectrum, planar fluence and angular distribution at the collim. Exit	THE+EXP
66	Wang and Li	Med. Phys. 28(2), February 2001	MC dose calculation of beta-emitting sources for intravascular brachytherapy: A comparison between EGS4, EGSnrc and MCNP	EGS4/EGSnrc and MCNP	DDCs and radial DDs (only calculations)	THE+CLI
67	Ye et al.	Med. Phys. Biol. 49(2004), 387-397	Benchmark of PENELOPE code for low-energy photon transport: dose comparisons with MCNP4 and EGS4	PENELOPE comp. to MCNP4C & EGS4	low energy photons of seeds (see Bohm) only simulative comparison - no meas.	THE
68	Zaidi	IEEE Trans on Nuc Sci 47(6), Dec. 2000	Comparative evaluation of photon cross-sections libraries for materials of interest in PET Monte Carlo simulations	Eidolon software diff. cross. Sect.	comp. for several human tissues and common det. materials from 1keV to 1MeV	THE

PROTON RADIATION CANCER THERAPY

**Wayne Newhauser
M.D. Anderson Cancer Center**

The most common cancer treatment strategies include surgery, chemotherapy, and radiation therapy. Proton beam radiotherapy, proposed in 1946 by Robert Wilson, offers the possibility to treat deep-seated tumors with large, uniform radiation doses, while simultaneously sparing adjacent healthy tissue, which is essential to minimize treatment related side effects. There are presently 24 proton centers operating worldwide, with another 11 coming on line in the next three years. Large-scale clinical trials are being planned in the United States to compare proton therapy with similar advanced treatment technologies, such as intensity-modulated photon radiation therapy.

Contemporary topics in radiation transport calculations in proton therapy may be classified in three major areas: treatment planning, therapy system design, and facility shielding design. In the early days of proton therapy, treatment planning was based on very simple 2-dimensional calculations. With the advent of three dimensional computed tomographic imaging devices in the 1970s, non-commercial 3-d treatment planning systems were developed. The dose algorithms in these first systems were simple broad beam algorithms, with minimal modeling of the transport physics such as lateral scattering. Some broad beam algorithms are still in clinical use today. Pencil-beam algorithms, originally developed for electron beams, were adapted to heavy charged particle beams in the early 1990s. The pencil beam algorithms are more physically realistic than broad beam algorithms, but require longer calculations times. Several companies have recently commercialized proton therapy treatment planning systems based on the pencil beam approach and calculations times are now considered acceptable for most routine treatment planning cases. The pencil beam algorithms contain approximations and simplifications that lead to significant discrepancies in cases with pronounced heterogeneities, especially in the presence of high-Z materials such as replacement hip joints. The Monte Carlo approach is widely acknowledged to be the most realistic in terms of modeling the radiation transport, and therefore, in theory, it should also be the most accurate. Monte Carlo has long been used to calculate dose in radiation protection studies involving high-energy protons, including space exploration and high-energy particle accelerator facilities. Recently, there have been several reports using general purpose (non-commercial) Monte Carlo codes, MCNPX, GEANT, and FLUKA to calculate dose distributions in various phantoms due to the primary therapy beam as well as from stray photon and neutron radiation. Contemporary implementations of these methods are still limited to research studies because of the long computation times required and a lack of comprehensive validation and testing data (i.e., FDA approval). We anticipate that all computation speed issues will eventually be resolved through improvements in affordable computing power, gains in execution speed from automatic variance reduction techniques, and other increases in computational efficiency. It is noteworthy that, for software used in the treatment of humans, the work associated with the validation is significant and may even exceed the software development effort. The availability of suitable benchmark test problems, along with experimental data, would help to substantially reduce this cost and barrier that many smaller research groups face. One recent (QUADOS) code intercomparison contained a low-energy proton therapy problem that was intentionally simple to maximize its tractability with wide variety of codes, although at the cost of clinical relevance. There remains a clear need for clinically useful benchmark

problems, i.e., with sufficient complexity and realism for testing the accuracy and speed of dose algorithms intended for human use.

In addition to codes that predict radiation transport, computational tools and benchmark tests are needed for such tasks as the conversion of computed tomography scans to material specifications, e.g., elemental composition and mass density for Monte Carlo codes. A separate group under the auspices of the ANS is working towards making available voxelized phantoms and related tools.

Proton therapy has recently undergone a transition for the research laboratory to the commercial marketplace. Vendors have legitimate concerns about their research and development costs, proprietary and confidential intellectual property, and protecting their unique advantages and offerings in a competitive marketplace. Because of these factors, we shall defer detailed discussions of computational activities pertaining to therapy system design and facility shielding design until a later time.

The research challenges in proton therapy are driven mainly by two main forces: the need to continue improving patient outcomes; and economic pressures to achieve cost competitiveness and cost effectiveness. Computer modeling and simulation will play an increasing role in achieving both these aims. Advanced predictive modeling technologies and computer technologies will be used to simulate radiation transport problems on macroscopic and microscopic scales. Key components will likely include Monte Carlo algorithms, parallel computing, benchmarking and validations, standardization (e.g., DICOM-RT-ION), automation and encapsulation, and simple human user interfaces.

Major applications will include patient-specific treatment planning, dose perturbations to sub-millimeter structures in the body, radiobiological modeling, and neutron shielding.

Some Issues in Proton Therapy Computations that are Common to Other Medical Applications

Typically, the geometric model used for the simulation must be prepared by the physicist or engineer who carries out the radiation transport simulations. For simple geometries, the existing general purpose Monte Carlo codes are well suited and convenient to use. However, modeling highly complex geometries is time consuming and prone to human error. Geometry visualization tools are distributed with the code packages as well as third party codes such as SABRINA and MORITZ, and these are essential in developing complex geometries. Several groups are working on conversion algorithms that would allow the use of solid-modeling programs such as SOLIDWORKS, commonly used in the field of computer aided design (CAD) and manufacturing (CAM), for creation of the simulation geometry. An automatic conversion capability would, to a large extent, streamline processes that include design, simulation, and construction phases.

Similarly, the specification of materials is laborious and prone to error. It would be helpful to have a standardized database of common structural, shielding, and biological materials that is freely available. There is a need for an open source research platform for performing treatment planning research and development work, such as the MINERVA system.

OVERVIEW OF DETERMINISTIC RADIATION TRANSPORT METHODS

M. L. Williams and R. A. Lillie*
Oak Ridge National Laboratory

I. INTRODUCTION

The stochastic Monte Carlo method often is considered to be the ultimate numerical approach for radiation transport calculations, especially for complicated geometries. However if differential distributions are required, then a deterministic solution of the Boltzmann transport equation is often more efficient. In therapy planning applications Monte Carlo calculations for 3D dose distributions in a voxel representation of a patient geometry can require an inordinate amount of computational time to obtain sufficient statistical accuracy at all important locations. This is especially true in regions of electronic disequilibrium where electron transport is necessary. While many medical physicists understand the basic principles underlying Monte Carlo codes such as EGS⁽¹⁾ and MCNP⁽²⁾, there is less appreciation of the capabilities of deterministic methods which in principle can provide comparable accuracies to Monte Carlo. Only within the last several years have serious studies been made of applying deterministic calculations to medical physics applications. In this paper we will present a general overview of deterministic methods and codes available for dose calculations, along with a survey of several previous applications in medical physics. The details of particular deterministic transport codes are described more fully by the other papers presented at the Workshop.

II. DESCRIPTIVE DERIVATION OF DISCRETE ORDINATES

The most versatile and widely used deterministic methods are variants of the discrete ordinates method. This method evolved from the “discrete S_N method” developed more than 40 years ago by B. G. Carlson and G. I. Bell at Los Alamos Laboratory^(3,4). This work was based on a similar technique that had been proposed earlier by Chandrashakr for astrophysics calculations.⁽⁵⁾ A number of multi-dimensional discrete ordinates production codes are currently available for radiation transport calculations, and have been used for a wide variety of reactor analysis, as well as shielding and dosimetric applications.⁽⁶⁻¹⁰⁾

The discrete ordinates method consists of subdividing the continuous six-dimensional phase-space domain of the Boltzmann equation into a set of discrete elements in space, energy, and direction. In therapy applications the spatial mesh usually corresponds to the rectangular voxel elements (or a combination of individual voxels) defined by the patient imaging procedure. To treat the energy variable, most discrete ordinates codes utilize the multigroup approximation which segments the continuous energy domain into intervals called “groups.” For example, in photon transport calculations, 20-100 groups could be used to describe an 18 MV energy spectrum. Nuclear data used in the transport calculations must be averaged over the appropriate energy intervals. Several such

* Retired

multigroup data libraries currently exist for neutron and photon interactions,^(11,12) but these have not been optimized for medical physics applications. Fortunately photon interaction data tend to have a simple variation versus energy, except at low energies where atomic binding effects cause structure in the photoelectric cross section. For example, Compton scattering is the predominant type of photon interaction for external beam therapy, and this cross section is described adequately by the free-electron Klein-Nishina formula, so that processing of an appropriate multigroup library is not difficult.

The most notable feature of the discrete ordinates method is that the directions traveled by particles are represented by a set of discrete direction intervals. This contrasts to other deterministic methods such as the spherical harmonics approach that uses an expansion in terms of basis functions to treat the angular coordinates of particle directions.⁽¹³⁾ The direction mesh can be represented by subdividing a unit direction-sphere into a number of area elements bounded by lines of latitude and longitude. The direction cosines defining a unit vector from the origin of the direction-sphere to the center of each surface element uniquely define the set of discrete directions. The solid angle subtended by each area element determines the “weight” (size) of the corresponding direction interval. The set of directions and weights is referred to as an S_N quadrature. The choice of directions and weights in most quadratures is constrained to preserve particle conservation in curved geometries and to produce invariant results under geometric transformations such as 90-degree rotations of the direction-sphere.

To derive the multigroup discrete ordinates equations, the continuous form of the Boltzmann transport equation, describing the particle flux distribution, is integrated over the previously defined phase space meshes to construct particle balances for each discrete phase-space cell. A complication arises due to the leakage terms appearing in the balance equations. For a given spatial cell, the unknowns appearing in the discrete ordinates equations are the particle fluxes averaged over the volume of the cell and the leakages through the cell surfaces. This is more unknowns than the number of balance equations available. Because the spatial mesh is swept in the direction of particle flow, the surface averaged fluxes representing particle flow *into* a cell are either known from earlier calculations of adjacent cells or from boundary conditions. The remaining unknowns representing particle flow *out of* each cell are eliminated by introducing auxiliary “differencing” relationships to provide closure for the number of unknowns. Differencing expressions relate the volume-averaged and the surface-averaged fluxes for a cell. The computation algorithm consists of solving the balance equation for the cell-averaged flux and then spatially extrapolating with the difference relationships to obtain the outgoing fluxes on the surface. In spherical and cylindrical coordinate systems, two additional unknowns arise due to “directional coupling,” corresponding to flow into and out of discrete direction intervals. These are handled with similar types of differencing relations.

Most production codes contain several alternative types of differencing relationships that may either be specified by the user or are selected internally by the program. The earliest and simplest to implement are the *diamond difference* relationships which treat cell averaged fluxes as a simple average of the appropriate incoming and outgoing surface fluxes. However, under certain conditions, these linear differencing relationships produced non-physical negative extrapolated fluxes. Hence less accurate (but always positive) differencing schemes such as the *linear-zero* and *linear-step* fixups were introduced to

circumvent these negatives whenever they occurred in the diamond-difference method. The more accurate/non-negative *weighted difference* relationships were later introduced. These difference relationships assumed the cell averaged fluxes could be well represented by a weighted average of the surface fluxes. In adaptive weighted diamond differencing, the weights are initially chosen to yield the standard diamond difference relationships and if negative extrapolated fluxes occur, new weights are determined using the latest calculated information. In the early versions of theta-weighted differencing, the source and both the space and angular transverse leakage terms appearing in the equations for the weights were multiplied by a parameter (theta) generally specified to be between 0.5 and 0.9 whereas in later versions only the transverse space terms were multiplied. In some very recent work, improved results were obtained when the value of theta was varied by direction. However, even when the weighted difference relationships are used, poor results and poor convergence can still occur in some problems. Because of this, still more complex linear nodal, linear-discontinuous, and characteristic methods were introduced.^(14,15) A number of variations in these higher order techniques have been proposed and implemented in several deterministic codes. Higher-order differencing approximations generally require more computational time per mesh element, but this is off-set by being able to use fewer spatial intervals.

The discrete ordinates solution algorithm consists of iteratively solving for the flux of particles within the phase space elements associated with each direction, space and energy grid. The flux of particles within the solid angle of a given quadrature direction is called the angular flux, while the sum over all directions is called the scalar flux. The transfer of particles between different energy groups and directions is mainly through scattering reactions. Many discrete ordinates codes represent the angular dependence of the scattering distribution using Legendre expansion coefficients, because the amount of interaction data stored in the library can be reduced. In this approach the discrete angular fluxes are converted to spherical harmonic "flux moments" that can be combined with the Legendre coefficients of the cross sections to compute the angular scattering source. The number of flux moments is usually less than the number of discrete angular fluxes, so the disk storage and memory requirements are reduced. A scattering reaction that changes a particle's direction, without causing sufficient energy loss to change groups, is called self-scatter. Over the years, a number of iteration acceleration methods have been developed and employed to improve convergence of the self-scattering source (inner iterations). Most of the early methods, i.e., power iteration, normalized power iteration, and Chebyshev, were extrapolation methods while most of the later methods, i.e., groupwise rebalance, space rebalance, partial current rebalance, and diffusion acceleration, are scaling methods. In the extrapolation methods, error estimates are obtained after a sufficient number of iterations and the current iterative values of the scattering sources are corrected. In the scaling methods, multiplicative factors are determined so that the most recently calculated particle fluxes may be scaled to achieve particle balance. Rapid convergence of the iterative procedure is very important for therapy planning, since many repetitive calculations are usually required for optimization studies.

In external beam therapy the uncollided component of the particle flux at given location is often the major contributor to the kerma. Auxiliary codes exist to calculate semi-analytic uncollided particle flux estimates and first-collision sources thereby eliminating or reducing "ray effects" that occur when isolated point sources exist in weakly scattering

media.⁽¹⁶⁾ The use of analytic first-collision methodology is very useful in treating the highly-collimated beams encountered in conformal therapy, and will be a necessary component in a practical deterministic code system for medical physics applications. This procedure requires efficient algorithms for performing ray-tracing in the voxel geometry.

III. DETERMINISTIC ELECTRON TRANSPORT

The discrete ordinates technique has been applied in neutron and gamma ray transport calculations for many years. The calculations for these two types of radiation are done very similarly, since they are both neutral particles. However therapy planning applications requires electron transport calculations to determine absorbed dose estimates in regions of electronic disequilibrium. Charged particle transport has several different features compared to the well established methods used for neutral particles.

In external beam therapy, secondary electrons are produced from ionizations by primary photon interactions-- usually Compton scattering. The absorbed dose is due to energy deposition in the medium by these free electrons, which cause ionizations and break chemical bonds to form free radicals that attack the functionality of cancer cells. Charged particle interactions are qualitatively different than neutral particle interactions. Whereas neutral particles must "hit something" to interact, free electrons interact through the long range Coulomb force. Most often the interaction occurs with distant orbital electrons, causing an excitation or ionization of the atom with little energy loss or change in direction by the free electron. This is called a soft inelastic reaction, which occurs essentially continuously because the electron always experiences a Coulomb force from the surrounding atoms. Alternatively the free electron may experience a catastrophic, close encounter with a bound electron, resulting in a wide-angle scatter and depositing a large fraction of its energy in the ejected electron. This reaction corresponds to a hard inelastic collision, which occurs rarely compared to soft-collisions, but deposits much more energy per event. Roughly half of the absorbed dose in radiation therapy is attributed to each mechanism.⁽¹⁷⁾ Hard and soft radiative interactions between energetic free electrons and the strong electric fields in the vicinity of atomic nuclei can also occur, producing secondary bremsstrahlung photons. Cross sections for these radiative inelastic reactions are large for high Z materials and high energy electrons; and thus may be important in computing x-ray source spectra from LINACS or in electron beam therapy, but are usually negligible for transport of Compton electrons in tissue. Electrons also scatter *elastically* from nuclei, causing erratic changes in direction with no energy loss.

Extension of the discrete ordinates method to address electron transport has been an active area of research for nearly twenty years. The conventional discrete ordinates technique of representing the angular scattering distribution by a Legendre expansion does not work well for soft inelastic interactions which are highly forward peaked. An alternative approach called the Fokker-Planck (FP) approximation represents the impact of soft reactions as continuously slowing down the electrons, while also continuously changing their direction; e.g., a mono-directional beam will be dispersed into a finite beam width. This approximation can be derived from a Taylor series expansion of the integrand in the scatter source term appearing in the Boltzmann equation, with the assumption that only small changes in energy and direction are significant.⁽¹⁸⁾ The resulting FP equation contains

derivatives with respect to energy and angular coordinates that are not present in the conventional transport equation. However the FP approximation is not accurate for treating hard interactions, which more closely resemble the discrete collisional scattering mechanisms encountered in photon and neutron transport. Therefore several studies have suggested incorporating the FP approximation to treat only the soft collisions appearing in the Boltzmann equation, while retaining the Legendre expansion of the hard-scattering source.⁽¹⁹⁾ The resulting expression is called the Boltzmann-Fokker-Planck (BFP) equation. Still another approximation used for deterministic electron transport is called the Boltzmann continuous-slowing-down (B-CSD) equation. This is similar to the BFP equation except that the continuous angular dispersion term is ignored, implying that soft reactions cause electrons to slow down continuously with no change in direction. The B-CSD equation is very analogous to the continuous slowing-down approximation in neutron transport theory, which leads to the Fermi age equation when diffusion theory is applied.

In order to obtain a deterministic solution to the electron transport equation, it would appear that currently available discrete ordinates codes must be modified to incorporate Fokker-Planck or CSD terms; and some of the newer discrete ordinates codes in fact do include energy and angular derivative terms for the FP method. However Morel has suggested that the FP/CSD terms may be incorporated indirectly into the transport solution by modifying the multigroup cross sections used in the discrete ordinates calculation; so that it is not necessary to modify the existing transport codes, but only the input data libraries.⁽¹⁸⁾ Using this approach Lorence and Morel developed a code called CEPXS to generate multigroup cross section data for coupled photon-electron discrete ordinate calculations with the B-CSD equation.⁽²⁰⁾ Later the methodology was extended in the CEPXS-BFP code to include the general FP terms with continuous angular dispersion.⁽²¹⁾ CEPXS also has the capability to produce coupled electron-photon cross sections. In the most general coupled library, photons produce electrons by Compton scatter, photoelectric absorption, and pair production (along with positrons); while electrons and positrons produce photons by radiative reactions, annihilation reactions, and fluorescence x-rays from atomic excitations. Several studies of deterministic radiation transport calculations for medical applications have used CEPXS to generate the necessary electron interaction data.

IV. EXAMPLE APPLICATIONS OF DETERMINISTIC TRANSPORT METHODS IN RADIATION THERAPY

Several papers have been published describing applications of the discrete ordinates method in radiation therapy. Reference 22 describes one-dimensional electron transport calculations performed at Louisiana State University (LSU) to determine the photon spectra for medical linear accelerator (LINAC) with varying electron energies and target compositions. The transport model consisted of a mono-directional electron beams with energies up to 18 MeV, impinging on targets consisting of varying thicknesses of copper and tungsten. The objective of the work was to determine the bremsstrahlung and characteristic x-ray spectra produced for clinical applications. The transport calculations were done with the ONEDANT discrete ordinates code⁽²³⁾ which is a 1D transport module in the DANTYS code system developed by LANL. This version of ONEDANT uses a higher order differencing method called the linear-discontinuous model, and is distributed by RSICC. CEPXS was used to process coupled electron-photon cross

sections so that the electron transport and photon production could be treated with the B-CSD approximation. Figure 1 shows a typical comparison of the emitted photon spectra computed by discrete ordinates and the MCNP Monte Carlo code. The agreement is very good, and the discrete ordinates calculations were about 60-900 times faster than Monte Carlo, depending on the statistical accuracy.

Reference 24 describes the use of the two dimensional discrete ordinates code TWODANT, another module in DANTYS, to determine kerma dose distributions for brachytherapy. Unlike external beam therapy, brachytherapy uses small radioactive seeds or other devices to place a radiation source within or very near the treatment volume. It is desirable therefore to localize the energy deposition to the treatment volume, and for this reason low energy photon or beta emitters are typically utilized as sources. In this case the depth-dose variation was calculated in a homogeneous water phantom, for ^{125}I and ^{192}Ir sources. It was assumed that the photon kerma adequately represents the absorbed dose for these relatively low energy sources, and hence no electron transport was performed. The seed was modeled in 2D cylindrical geometry, and a first collision source within the surrounding medium was computed by an auxiliary code. Figure 2 compares kerma doses computed by Monte Carlo and discrete ordinates using a 42 and a 210 group cross section library. Generally the agreement is within a few percent, and the deterministic computations were found to run 2-5 times faster. It was found that the calculated dose distribution is sensitive to the multigroup energy structure. The authors conclude that for brachytherapy applications the group structure should be optimized to adequately represent important photoelectric cross section discontinuities (K, L, and M edges).

Another widely used discrete ordinates code system is DOORS⁽⁶⁾, which includes ANISN (1D)⁽²⁵⁾, DORT(2D)⁽¹⁵⁾, and TORT(3D)⁽²⁶⁾ transport codes. The accompanying paper by Lillie presents a survey of several medical physics applications using DOORS transport computations, including a recent study that compares 3D TORT and Monte Carlo photon transport results in a voxel representation of a patient, obtained from a CT imaging file. In addition to the 3D kerma results described in Lillie's paper, coupled photon-electron transport calculations have also been performed with the 1D ANISN code to determine the fluxes for a linear slice through the patient geometry; i.e., a single row of voxels going from front to rear, and passing through both high and low density tissue. Multigroup, coupled photon-electron cross sections for the transport calculations were processed by the CEPXS-BFP code.⁽²¹⁾ A representative LINAC photon source spectrum was placed on the left side of the model. Of course the one dimensional slab geometry does not allow any flux variation transverse to the beam, but the depth dependence of the photon and electron fluxes provides a useful test case for the methodology. Figure 3 compares the total electron fluxes computed by ANISN using three different order quadratures, and those obtained from Monte Carlo reference calculations with EGSnrc and MCNP, respectively. There is some uncertainty in the reference results, as the two different MC codes do not produce entirely consistent values; i.e., the EGSnrc calculated total electron fluxes are approximately 5 % lower than those obtained from MCNP. It can be seen that the lower order S16 ANISN results exhibit a somewhat different spatial variation compared to Monte Carlo; however the S32 and S64 deterministic transport results agree well with the MCNP values. It is quite possible that the absorbed dose can be computed deterministically even more accurately

than the total flux results shown here, since the low energy electron fluxes have the most disagreement.

Other deterministic transport codes have also been examined for potential medical physics applications. Several of these codes use advanced variations of the original discrete ordinates method implemented in traditional code systems such as DOORS and DANTYS.

PENTRAN is a 3D discrete ordinates code that has been developed especially for execution in parallel computational systems.⁽⁸⁾ In the past PENTRAN has been used mainly for reactor shielding and core calculations, but recently researchers at the University of Florida have been extending its capability to address medical applications.⁽²⁷⁾ The accompanying Workshop paper by Sjoden describes the PENTRAN code in more detail.

The ATTILA code is based on work done at LANL to develop a finite-element transport method for unstructured tetrahedral meshes, providing the capability to model complex 3D geometry.⁽²⁸⁾ A feature of ATTILA that makes it attractive for medical physics is that it directly includes the CSD term, so that electron transport can be treated.

The TransMed code developed by Transware, Inc. is based on a deterministic formulation called the Method of Long Characteristics.⁽⁹⁾ It uses quadrature directions similar to the standard discrete ordinates method, except the solution algorithm constructs a series of parallel rays throughout the 3D geometry. The neutron balance equations are determined for the “tubes” defined by the parallel rays as they pass through the geometric bodies. The interactions of the rays with the body surfaces are done using Monte Carlo ray tracing routines, so that this method allows a very general geometric modeling capability. The basic code has been supplemented by analytic first collision routines.⁽²⁹⁾ The Workshop paper by Sajo and Williams describes example photon transport calculations performed using TransMed for a LINAC configuration with beam shaping devices.

SUMMARY

Deterministic solutions of the transport equation have the potential of providing 3D dose distributions with comparable rigor as Monte Carlo methods, but with no statistical “noise” in the results. Advances in computational methods for addressing electron transport and improvements in computation efficiency are needed before the techniques are practical for clinical therapy planning. Several radiation transport groups are currently engaged in developing and testing advanced deterministic approaches for medical physics work.

REFERENCES

1. I. Kawrakow, “Accurate Condensed History Monte Carlo Simulation of Electron Transport. I: EGSnrc, the new EGS4 version,” *Med. Phys.* **27**, 485 (2000).
2. J. F. Briesmeister, Ed., *MCNP – A General Monte Carlo N-Particle Transport Code*, Los Alamos National Laboratory report LA-12625-M, (1993).

3. B. G. Carlson, *Solutions of the Transport Equation by SN Methods*, Los Alamos National Laboratory report LA-1599, (1953).
4. B. G. Carlson and G. I. Bell, *Proc. of Second Conference on Peaceful Uses of Atomic Energy*, **16**, 535 (1958).
5. S. Chandrasekhar, *Radiative Transfer*, Oxford University Press, 1950.
6. *DOORS3.1 – One, Two- and Three Dimensional Discrete Ordinates Neutron/Photon Transport Code System*, Radiation Safety Information Computational Center (RSICC) Code Package CCC-650, Oak Ridge, TN (1996).
7. *DANTSYS 3.0, One, Two, and Three Dimensional Multigroup, Discrete Ordinates Transport Code System*, RSICC Computer Code Collection CCC-547, Oak Ridge National Laboratory (December 1992).
8. G. Sjoden and A. Haghghat, “PENTRAN: Parallel Environmental Neutral Particle Transport, Users Guide to Version 9.00,” *H&S Advanced Computing Technologies* (2000).
9. *TransMED Medical Physics Software, User’s Manual*, TransWare Enterprises, Inc., San Jose, CA, (Oct. 2000).
10. C.R.E.Oliveira and A.J.H. Goddard “EVENT- A Multidimensional Finite Element-Spherical Harmonics Radiation Transport Code,” in *OECD Proceedings, 3-D Deterministic Radiation Transport Computer Programs. Features, Applications and Perspectives*. 2–3 Dec. 1996, OECD Chateau de la Muette, Paris, France.
11. J. E. White, *et al.*, “VITAMIN-B6: A Fine-Group Cross Section Library Based on ENDF/B-VI for Radiation Transport Applications,” *Proc. Int. Conf. Nucl. Data Sci. & Tech.* Gatlinburg, TN (1994).
12. *BUGLE-96: Coupled 47-Neutron, 20-Gamma Ray Group Cross Sections Library Derived from ENDF/B-VI for LWR Shielding and Pressure Vessel Dosimetry Applications*, RSICC data collection DLC-185, Oak Ridge National Laboratory (1996).
13. G. I. Bell and S. Glasstone, *Nuclear Reactor Theory*, Van Nostrand Reinhold Co., N.Y., 1970.
14. R. D. O’Dell and R. E. Alcouffe, *Transport Calculations for Nuclear Analysis: Theory and Guidelines for Effective Use of Transport Codes*, Los Alamos National Laboratory report LA-10983-MS, (1987).
15. W. A. Rhoades and R. L. Childs, “The DORT Two-Dimensional Discrete Ordinates Transport Code,” *Nucl. Sci. & Engr.*, **99**, 88–89, (1988).
16. R. A. Lillie, “GRTUNCL3D: A Discontinuous Mesh 3-D First Collision Source Code,” *Proc. Am. Nucl. Soc. RP&S Div. Top. Conf.*, Nashville, TN (1998).
17. F. H. Attix, *Introduction to Radiological Physics and Radiation Dosimetry*, John Wiley & Sons, N.Y., 1986.

18. J. E. Morel, "Fokker-Planck Calculations Using Standard Discrete Ordinates Transport Codes," *Nuc. Sci. Eng.*, **79**, 340–356 (1981).
19. M. Landesman and J. E. Morel, "Angular Fokker-Planck Decomposition and Representation Techniques," *Nucl. Sci. Engr* **103**, 1 (1989).
20. L. J. Lorence, J. E. Morel, and G. D. Valdez, *Physics Guide to CEPXS: A Multigroup Coupled Electron-Photon Cross Section Generating Code*, Sandia National Laboratory report SAND89-1685, (October 1989). Also described in RSICC Computer Code Collection CCC-544, Oak Ridge National Laboratory (December 1992).
21. A. M. Voloschenko, *CEPXS-BFP: Version of Multigroup Coupled Electron-Photon Cross Section Generating Code CEPXS, Adapted for Solving the Charged Particle Transport in the Boltzmann Fokker-Planck Formulation with the Use of Discrete Ordinates*, Keldysh Institute of Applied Mathematics, Russia, report, KIAM Report No. 7-36-2004, (2004).
22. M. L. Williams and E. Sajo, "Deterministic Calculations of Photon Spectra for Clinical Accelerator Targets," *Med. Phys.* 29 (6): 1019-1028 (2002).
23. R. D. O'Dell. *Revised Manual for ONEDANT: A Code Package for One-Dimensional Diffusion-Accelerated Neutral Particle Transport*, Los Alamos National Laboratory report LA-9184-M, Rev. December, 1989.
24. G. M. Daskalov, *et al.*, "Two-Dimensional Discrete Ordinates Photon Transport Calculations for Brachytherapy Dosimetry Applications," *Nucl. Sci. Engr* **134**, 212 (2000).
25. W. W. Engle, Jr., *ANISN, A One-Dimensional Discrete Ordinates Transport Code with Anisotropic Scattering*, ORGDP Report K-1693, Oak Ridge, TN (1967).
26. W. A. Rhoades, *The TORT Three-Dimensional Discrete Ordinates Neutron/Photon Transport Code*, ORNL Report ORNL/TM-13221, Oak Ridge, TN (1996).
27. A. Al-Basheer, M. Ghita, G. Sjoden, and B. Dionne, "Critical Discretization Issues in a 3D Discrete Ordinates Medical Physics Simulation Benchmarked with Monte Carlo," presented at the ANS 14th Biennial Topical Meeting of the Radiation Protection and Shielding Division, Carlsbad, N.M., April 2–6, 2006.
28. T. A. Wareing, J. M. McGhee, and J. E. Morel, "ATTILA: A Three-Dimensional Unstructured Tetrahedral Mesh Discrete-Ordinates Transport Code," in *Proceedings of the American Nuclear Society Annual Winter Meeting, Washington, D.C., November 10–15 1996*.
29. M. L. Williams *et al.* "Deterministic Photon Transport Calculations in General Geometry for External Beam Radiation Therapy." *Med Phys* **30** (12) 3183–3195 (2003).

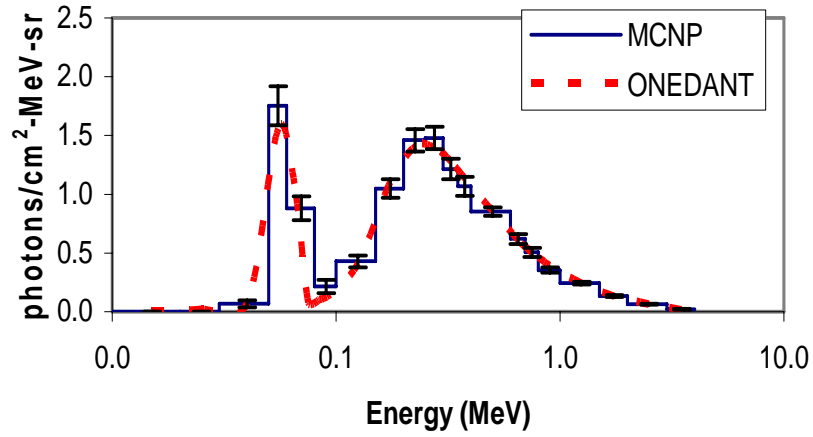


Figure 1. Calculated Photon Emission Spectrum Produced by Electron Linear Accelerator. Taken from M. L. Williams and E. Sajo, "Deterministic Calculations of Photon Spectra for Clinical Accelerator Targets," *Med. Phys.* 29 (6): 1019-1028 (2002).

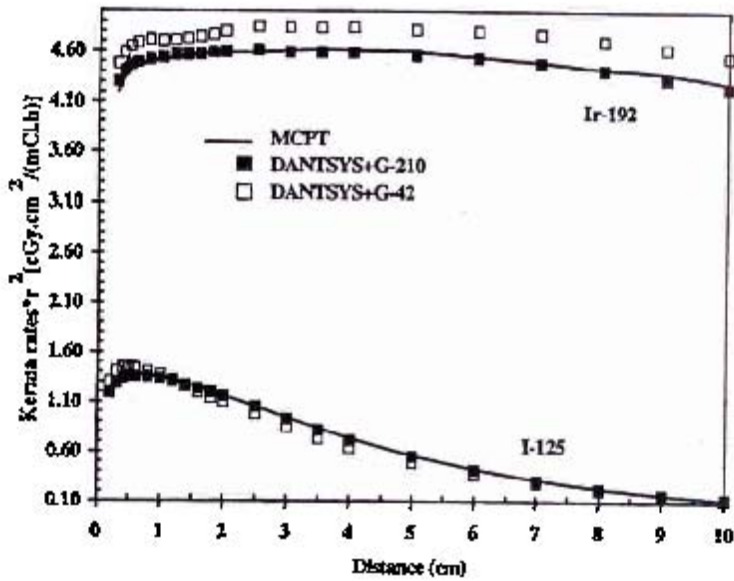


Figure 2. Calculated Kerma Dose Distributions

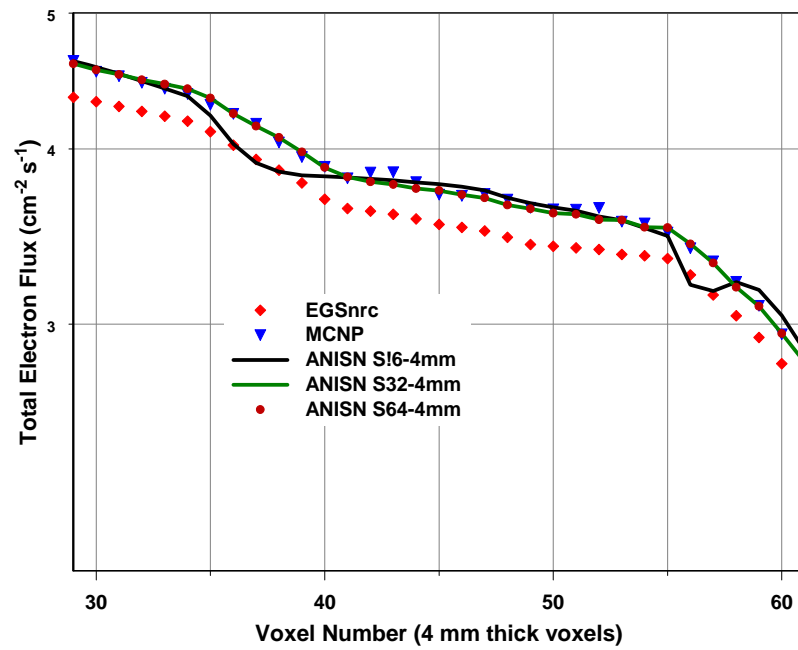


Figure 3. Comparison of Electron Fluxes Computed by Monte Carlo and Deterministic Methods

DOORS RADIATION TRANSPORT CODE SYSTEM

R. A. Lillie[†]

Oak Ridge National Laboratory

I. INTRODUCTION

DOORS¹ is a collection of codes anchored by the one- two- and three-dimensional discrete ordinates transport codes, ANISN², DORT³, and TORT⁴, respectively. Pre- and post-processing codes are included in the collection to prepare cross-section data, pass data from one code to another, and help interpret calculated results. Two- and three-dimensional semi-analytic uncollided flux and first collision source codes and a two-dimensional last flight estimation code are available to help reduce some of the problems that arise in large low scattering regions. Coupling codes that allow extremely large problems to be run using bootstrapping techniques are also included in DOORS. These coupling codes allow complex three-dimensional structures embedded in large two- or three-dimensional geometrically simple zones to be efficiently treated using more than one transport code. In addition, graphics codes together with a graphics library are included in DOORS to generate contour plots of particle flux or specified responses.

In Sections II through IV, a limited survey of DOORS use in medical applications is presented. A number of investigations directed at optimizing Boron Neutron Capture Therapy (BNCT) facility designs are described in Section II. Doses calculated with DOORS in a portion of a human leg are compared against those obtained from Monte Carlo calculations in Section III and fluxes calculated with DOORS in a dog head phantom are compared against both measured and Monte Carlo calculated fluxes in Section IV. Finally, in Section V, the results from a very recent study comparing DOORS and Monte Carlo calculated fluxes and energy depositions resulting from a high energy photon beam incident on a CT based human phantom model are presented and discussed.

II. BNCT FACILITY DESIGN OPTIMIZATION

ANISN and DORT have been used at a number of institutions to optimize material selections for Boron Neutron Capture Therapy beam filter designs. Both “brute force” optimizations and optimizations using gradient information have been performed. BNCT is a bimodal therapy first proposed over 50 years ago as a means of treating malignant brain tumors, in particular, glioblastoma multiforme (GBM). In BNCT, the patient is first given a suitable boronated pharmaceutical that preferentially seeks the malignant tissue. The tumor region is then irradiated with an epithermal or near epithermal neutron beam to generate a thermal fluence in the diseased tissue. Due to the high ¹⁰B thermal neutron capture cross section, the ¹⁰B readily absorbs a neutron. It then breaks up into two charged ions (⁴He & ⁷Li) that range out over cellular dimensions thereby enhancing the destruction of tumor tissue with minimal dose to the surrounding healthy tissue. In what follows, BNCT optimizations performed employing one-dimensional methods are first discussed. A multidimensional optimization method is then discussed.

A. One-Dimensional Calculations

Ingersoll, Slater, and Williams⁵ performed several one- and two-dimensional analyses using ANISN and DORT to determine if the Tower Shielding Reactor (TSR-II) at Oak Ridge

[†] Retired

National Laboratory (ORNL) could provide a suitable beam for BNCT. In their analyses, they investigated the use of a number of materials commonly considered in BNCT filter designs, e.g., aluminum, heavy water, sulfur, bismuth, lead, cadmium, boral and lithiated polyethylene, and found the best balance between beam intensity and energy spectrum could be obtained using an aluminum/aluminum fluoride material.

Their preliminary one-dimensional calculations led to a beam filter design consisting of 0.8 m of Al/AlF₃ (in a 1:1 mixture) followed by 92 mm of sulfur, 0.2 mm of cadmium, and 0.1 m of bismuth. Two-dimensional calculations then indicated that a 0.1-m-thick lithiated polyethylene collimator provided acceptable beam definition with minimal beam loss. The calculated patient incident epithermal flux and beam purity (ratio of epithermal current divided by four times the fast neutron kerma plus photon free-in-air tissue kerma) for this design indicated that a beam having a magnitude and spectral purity comparable to other proposed BNCT facilities could be obtained at the TSR-II.

In addition to the above work, a large number (too large to be referenced here) of other investigators have also employed ANISN to design possible BNCT facilities since this code is extremely fast and thus well suited for preliminary or conceptual design calculations.

The TSR-II beam filter design was achieved using “brute force” methods, i.e., by manually varying the different materials until an acceptable filter was obtained. Other investigators, in particular, Karni, Greenspan, Vujic, and Ludewigt,^{6,7} have utilized gradient information to help select optimal materials for use in BNCT facilities.

Karni and Greenspan⁶ investigated the feasibility of using the SWAN⁸ optimization code to identify suitable neutron source assemblies for BNCT applications. SWAN uses gradient information to calculate material replacement effectiveness functions. The material replacement effectiveness function of material *j* relative to a reference material *k* predicts the change in a performance parameter due to the replacement of material *j* by an equal amount of material *k* at a given location. SWAN is based on a perturbation theory approach and as such requires the calculation of both forward and adjoint fluxes. In their investigation, these fluxes were obtained employing the one-dimensional discrete ordinates transport code ANISN.

At the time of their investigation SWAN could only be used to optimize linear functionals. However, BNCT material optimization generally requires the optimization of a ratio of functionals, i.e., the ratio of the damage rate or dose in a tumor to that in some selected healthy tissue near the tumor. To overcome this problem they developed a strategy that consisted of calculating the forward flux and two adjoint fluxes, i.e., one for the numerator and one for the denominator. This allowed them to easily obtain from SWAN a material replacement effectiveness function versus position for the ratio of responses by subtracting the effectiveness function for the denominator from that for the numerator.

The one-dimensional model employed in their study consisted of an inner 40 cm thick alumina reflector, a 1 cm thick isotropic neutron source region, and a 40 cm thick beryllia moderator. Immediately outside the moderator, a layer of ⁶LiF separated 18 cm of healthy tissue that was assumed to contain a tumor loaded with ¹⁰B. In the optimization, Al₂O₃, BeO, Be, D₂O, H₂O, C, MgO, SiC, CaCO₃, ⁷LiF, ⁶LiF, and Pb were allowed to replace the initial reflector and moderator materials and the concentration of the ⁶LiF was allowed to vary.

The optimization strategy chosen by the authors to illustrate the use of SWAN consisted of first selecting promising constituents based on the calculated material replacement effectiveness functions. Once promising constituents were identified and substituted for the

original reflector and moderator materials, they searched for optimal constituent distributions by analyzing calculated material replacement effectiveness functions for the new reference configuration. Although the results from their investigation may not be directly applicable to actual BNCT treatment facilities since only one-dimensional models were employed, their study did demonstrate the feasibility of using SWAN. In addition, (and probably more important), some if not many of the material changes predicted by SWAN would most likely not have been predicted by even an experienced BNCT facility designer.

In a separate study⁷, Karni and Greenspan together with Vujic and Ludewigt illustrated the use of SWAN in identifying optimal beam shaping assemblies for two accelerator energies. Their results indicated that SWAN could be used to reliably compare different BNCT facility designs.

B. Multi-Dimensional Calculations

Shortly after the one-dimensional optimization efforts described above, a multi-dimensional optimization strategy for BNCT filter design including a local (versus global) optimizer was developed by Lillie⁸ at Oak Ridge National Laboratory. The optimizer employed a fairly simple quasi one-dimensional line search based on gradient information obtained using forward and adjoint fluxes calculated with the two-dimensional transport code DORT.

The overall optimization strategy consisted of first calculating two adjoint leakages from a patient's head using the three-dimensional transport code TORT. The adjoint sources for these calculations consisted of dose response functions distributed over the tumor volume and over the healthy brain tissue between the tumor and the beam entrance to the head. After processing these leakages into source terms, the optimization code was executed through system calls to the DORT code to obtain one forward and two adjoint flux distributions throughout a two-dimensional beam tube-filter (BTF) geometry. These flux distributions were then used to obtain the gradient of the dose ratio (dose in tumor divided by dose in healthy tissue) with respect to the materials comprising the BTF geometry.

The optimizer was initially tested using two fairly simple one-dimensional models. The leakage spectrum from the TSR-II was chosen as the radiation source for both test cases. In the first test, epithermal to non-epithermal (including photon) flux ratios were maximized. The initial filter compositions consisted of one of six candidate materials, i.e., either LiF, D₂O, Pb, Be, Al₂O₃, or Cd. After optimization, improvements in the flux ratios ranged from 1.5 to over 200. This wide range readily illustrates that the optimizer could only search for local maximums. In the second test, the final "brute force" filter design given above for the TSR-II was chosen for the initial filter composition. After optimization, increases of between 26 and 43 percent in beam purity were obtained using three different criteria to select changes in composition during each step of the optimization search.

In the final test of the optimization strategy, a patient's head was simulated using a simple three-dimensional parallelepiped model and a small tumor was placed in the center of the model. The initial BTF geometry consisted of a 1 m thick filter having a 0.2 m radius which was in turn surrounded by 0.05 m thick beam tube comprised of a 50-50 mixture of Be and lithiated paraffin containing 7.5 weight percent Li. The filter consisted of 0.6 m of a 25-75 mixture of Al and AlF₃, 0.2 m of Al at 75 percent theoretical density, 0.1 m of AlF and Bi at 10 and 35 percent theoretical density, respectively, and 0.1 m of Bi at full density. This filter design was based on the final filter compositions from the second test case. As in the simple tests, the TSR-II spectrum was employed as the radiation source.

In this final test, adjoint leakages from the patient's head were first calculated using TORT. Adjoint sources equal to tumor and healthy brain tissue kerma, assuming 30 ppm natural B in the tumor and 3 ppm in the healthy tissue, were employed in these calculations. Inspection of the adjoint leakages indicated that only neutrons with energies between 100 eV and 100 keV can produce tumor-to-healthy-tissue dose ratios greater than 1.0. In addition, only neutrons with energies between 10 and 40 keV can produce a maximum possible dose ratio of 1.33. The low maximum possible dose is due to the use of natural B (not enriched) and due to the tumor being located more than a few cm from the surface of the head where BNCT is most effective. After optimization, the neutron flux between 100 eV and 100 keV at the filter exit increased by almost a factor of 200, whereas over the remainder of the spectrum the maximum increase was less than a factor of 40. This spectral shift after optimization increased the tumor to healthy tissue dose ratio from 0.78 to 1.17. Thus the optimization strategy was successful in increasing the dose ratio from approximately 59 to 88 percent of the maximum possible dose ratio.

III. LOWER LEG DOSE COMPARISON

Ingersoll, Slater, Williams, Redmond, and Zamenhof⁹ have compared dose distributions obtained with TORT with those obtained from the Monte Carlo code MCNP.¹⁰ The primary purpose of their study was to assess the relative computational merit of a deterministic transport code against a stochastic transport code.

Their comparison was performed using a voxel model of a lower leg built from computed tomography (CT) images with the MCNP model containing 11,025 voxels and the TORT model containing 15,782 voxels. The increased number of voxels in the TORT model was required since TORT requires its parallelepiped mesh to extend over the entire geometric model. They varied a number of input parameters to both codes and used cross-section data based on Versions V and VI of the Evaluated Nuclear Data File (ENDF). They observed very little difference with the choice of cross sections. However, they found that the use of $S(\alpha,\beta)$ scattering kernels in MCNP greatly improved the comparison between the two codes. They also found that most of the parameter changes in TORT produced relatively minor differences in calculated doses whereas a fairly significant differences appeared in the MCNP calculated doses when the number of histories was increased from 3 to 10 million.

Running times for those cases in which better than 5 percent agreement was found to exist in more than 95 percent of comparable voxels (not all of the TORT voxels were in the MCNP model) indicated that TORT was nearly a factor of 15 times faster than MCNP. It was clear from their study that TORT provided an excellent alternative to Monte Carlo methods for BNCT treatment planning when voxel-based anatomical models were employed.

IV. PHANTOM DOG HEAD COMPARISON

Wheeler and Nigg¹¹ have performed numerous studies in which they compared calculated dose distributions in a lucite dog head phantom using both stochastic and deterministic methods against measured data. The measured data was obtained using the existing Brookhaven Medical Research Reactor (BMRR) beam at Brookhaven National Laboratory. In addition to comparisons to measured data, they also performed calculations to evaluate important dose parameters for the proposed Power Burst Facility beam at Idaho National Engineering Laboratory (INEL). In their comparisons, the stochastic calculations were carried out using the Monte Carlo module rtt_MC under development at INEL and the deterministic calculations were carried out using TORT.

To obtain their measured data, they activated copper-gold alloy wires in catheters that had been inserted into vertical pre-drilled holes in the dog head phantom. This alloy was chosen so that the thermal flux could be measured separately from the total flux.

The dog head phantom was irradiated with the beam incident on the top center of the phantom and all normalizations were performed based on a nominal BMRR power of 2.9 MW. The vertical thermal flux profiles obtained from both calculational methods through the phantom at the center of the beam agreed with the measured profile within 15 percent or better. The peak thermal flux obtained from the Monte Carlo calculation was approximately 12 percent greater than the measured value whereas the TORT calculated peak thermal flux was only approximately 6 percent greater. The TORT calculation did however require more than three times as much computation time. In spite of the increased run time, Wheeler and Nigg conclude that deterministic codes such as TORT are very well suited for BNCT applications.

V. PHOTON-ONLY HUMAN PHANTOM COMPARISON

Recently, photon-only deterministic transport calculations were performed to obtain flux and energy deposition distributions throughout a human phantom lung model using the 3-D discrete ordinates transport code TORT. Results from these calculations were subsequently compared to similar results obtained using EGSnrc¹². The phantom lung model was based on reformatted CT scan data obtained from the Department of Radiation Oncology at the University of North Carolina (UNC) at Chapel Hill. The geometry employed in these comparative calculations consisted of 124 x 62 x 75 cubic 4 mm voxels containing water. The density in each voxel was taken to be the CT number (0-4095) divided by 1000. A few planes of this CT data set are shown in Figure 1. Special routines were written to prepare the geometry data for TORT and EGSnrc. In addition, a voxel geometry package was written to perform the particle tracking in EGSnrc. In order to compare with the discrete ordinates in a consistent manner, electron transport was turned off in EGSnrc by setting the electron cutoff energy well above the highest source photon energy thus causing all electrons created in a voxel to be immediately absorbed in that voxel.

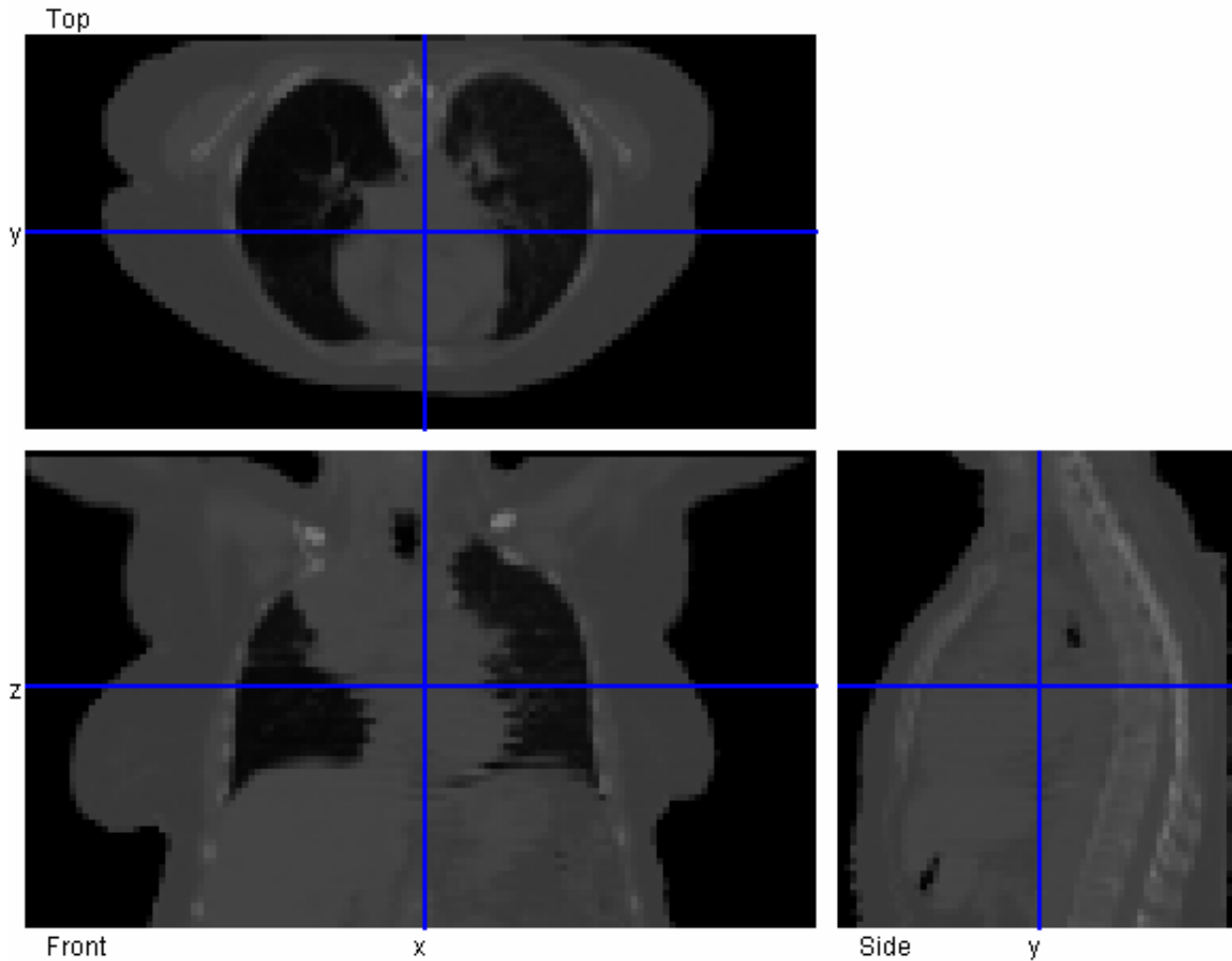


Figure 1. CT Images from CT Data Set used in the TORT/EGSnrc

The photon source employed in both the discrete ordinates and MC calculations was represented by a single isotropic source located 100 cm from the CT scan isocenter and consisted of collimated and scattered components. The collimated beam component contained 0.77 photons and was isotropic within the solid angle subtended by a 10 x 10 cm square centered at the scan isocenter. The scattered or background component contained 0.23 photons and was also isotropic but extended over the solid angle subtended by a 35.35 cm radius disk similarly centered. Thus, all of the deterministic and MC calculations were consistently normalized to one source photon. The energy distribution of both components was derived from previously calculated phase space data also supplied by UNC.

The cross sections employed in the EGSnrc calculations were processed directly from the continuous energy cross section data supplied with EGSnrc. The cross sections employed in the discrete ordinates calculations were taken from the VITAMIN-B6 fine group library¹³ and consisted of the 40 lowest photon energy group cross sections (photon data for energies below 14 MeV). In this library, all photon scattering is represented using P_5 Legendre expansions to represent angle-to-angle transfers. Legendre polynomials are used to represent the directional dependence of scattering in discrete ordinates codes since scattering is only dependent on the cosine of the angle between the incident and scattered directions. These polynomials form a complete set of orthogonal basis functions over the range [-1,1]. Photon kerma factors from the VITAMIN-B6 library were used to convert

photon flux from TORT into energy deposition. The energy deposited in the MC calculations was obtained directly by scoring the collisional energy lost of the sampled photons, whereas track length estimation was used to obtain the flux.

In the EGSnrc calculations, the source was simply sampled from both distributions (collimated and scattered) with rejection techniques employed to define the square beam. Photon-only transport was accomplished by setting the electron low energy cut at 100 MeV which is well above the maximum beam photon energy of 14 MeV. Thus, any electrons produced are immediately absorbed and their energy is deposited. In the deterministic calculations the source was input into a slightly modified version of the code GRTUNCL3D.¹⁴ This code calculates the energy and angular dependent uncollided fluxes throughout the TORT geometric model and folds these fluxes with the Legendre expansion coefficients of the scattering cross sections to obtain first-collision source moments that are in turn input to TORT. TORT proceeds in transporting the photons emanating from the Legendre expansion of the first-collision source represented by the moments to compute collided fluxes. The total energy dependent photon flux throughout the patient/phantom geometry is then obtained by simply adding the collided fluxes from TORT to the uncollided fluxes from GRTUNCL3D.

Transverse profiles of the total (integrated over energy) photon flux and the energy deposited obtained using discrete ordinates and MC are shown in Figures 2 and 3, respectively. In both figures, the results from EGSnrc are represented by red dots whereas the results from the discrete ordinates calculations are represent by solid and broken lines. Six separate discrete ordinates calculations were performed and these are denoted in the legend with TORT followed by “p5 full”, “p5 2 iter”, “p5 1 iter”, “p3 full”, “p3 2 iter”, and “p3 1 iter”. P_5 and P_3 signify the order of the Legendre expansion of the scattering cross sections and “full”, “1 iter”, and “2 iter” signify whether the TORT calculation was run to completion, i.e., full convergence, or whether they were terminated after either one or two iterations. The reason calculations were performed using only one or two iterations is that these calculations produce collided fluxes due to particles that have collided only once (“1 iter”) or that have collided only once or twice (“2 iter”).

Both the flux and energy deposited profiles obtained from the TORT P_5 full convergence and the P_5 two iteration calculations agree very well with the EGSnrc results. In general, they lie within 1-2 standard deviations of the MC results except at the beam edge. At these locations large differences occur as GRTUNCL3D only estimates to cell centers and the uncollided flux may be either high or low depending on whether a specific voxel center lies inside or outside the beam path. (This is not a serious problem, however, since GRTUNCL3D may be easily modified to treat voxels that are only partially in a beam). The energy deposition profile obtained from the TORT P_5 single iteration calculation agrees within 25% of the MC results, however the flux profile obtained from this TORT calculation underestimates the MC result outside of the beam by up to 40%. The reason for the better agreement in the energy deposited profiles is because the higher energy photons, which do not collide many times before exiting the phantom, contribute more heavily to the energy deposition whereas both the high and low energy photons contribute with equal weight to the flux. The flux and energy profiles from the TORT P_3 calculations (fully converged, single iteration, and double iteration) compare very well within the beam but tend to overestimate the flux by up to 50% and energy deposited by up to 20% outside the beam because the P_3 scattering expansion is not high enough order to properly describe forward peaked scattering, thereby causing more large-angle scattering, that forces more particles out of the beam.

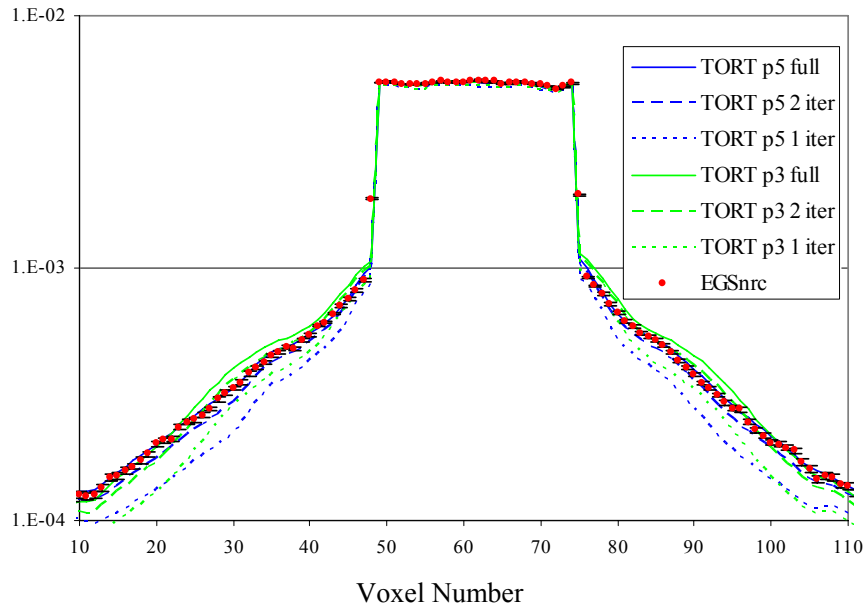


Figure 2. Discrete Ordintates vs Monte Carlo Flux Transverse Profiles on a Mid-plane Coronal Slice halfway between CT Isocenter and Beam Exit

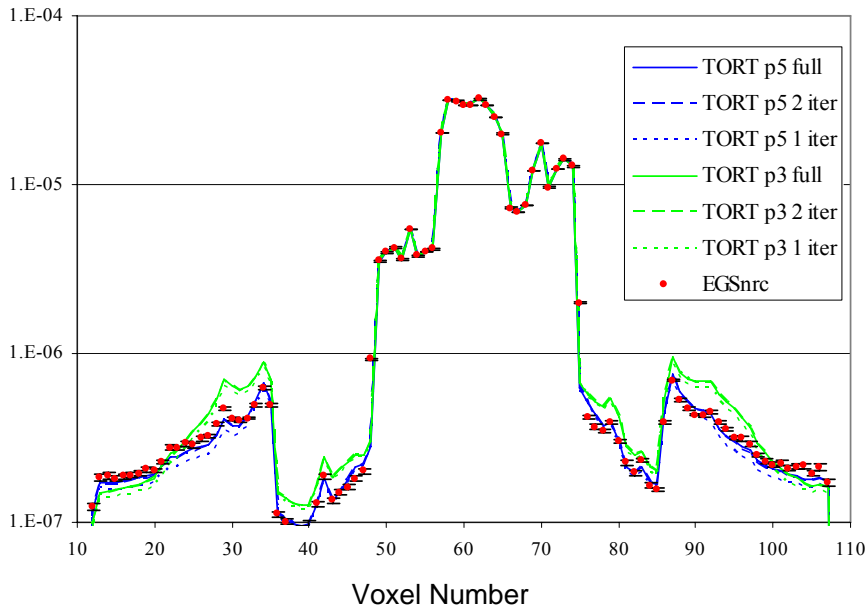


Figure 3. Discrete Ordintates vs Monte Carlo Energy Deposited Transverse Profiles on a Mid-plane Coronal Slice halfway between CT Isocenter and Beam Exit

The significant point to note regarding these comparisons is that since energy deposited is directly proportional to kerma (which is equal to absorbed dose in regions of electronic equilibrium), it may be possible to obtain adequate representations of photon flux and thus scattered and produced electrons and to a lesser extent produced positrons deterministically with only a few iterations thus reducing the photon transport computational cost even more.

The location of the transverse flux and energy deposition profiles was chosen to illustrate how well the discrete ordinates and MC calculations compare at a depth sufficient to see the effects of particle scatter within the beam. However, these profiles only present data along one row of voxels and thus depict only fairly localized differences between the two methods. To illustrate differences between the discrete ordinates and MC calculated results on a more global or overall basis, the difference between the discrete ordinates and MC calculated total flux and energy deposited in each voxel was divided by the corresponding MC uncertainty for that voxel. This ratio should provide a good measure of how well the discrete ordinates calculated result is matching the MC result. Determining these ratios for every voxel and then determining their frequency, (i.e., how many voxels have ratios between 0 and 1, 1 and 2, etc., MC standard deviations), yields a measure of overall agreement.

The fractional frequency distributions, i.e., the number of voxels having a given ratio divided by the total number of voxels, are shown in Figures 4 and 5 for the calculated total fluxes and energies deposited, respectively, for all six discrete ordinates calculations. These distributions reinforce on a global scale the conclusions drawn from the above profile comparisons. In general, the discrete ordinates calculations performed with P_3 scattering expansions tend to underestimate both the total flux and energy deposited much more often than those performed with P_5 cross sections. More important, the TORT P_5 two iteration calculation produces a distribution very similar to the TORT P_5 fully converged calculation, thereby also reinforcing the possibility of obtaining adequate photon flux distributions deterministically without much computational cost.

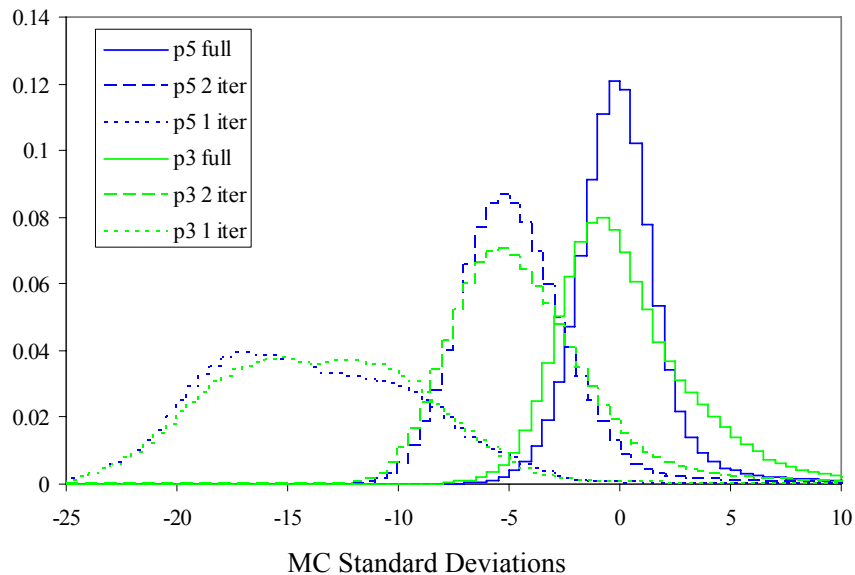


Figure 4. Fractional Frequency Distribution of Voxel Flux Differences between Discrete Ordinates and Monte Carlo divided by MC Standard Deviation

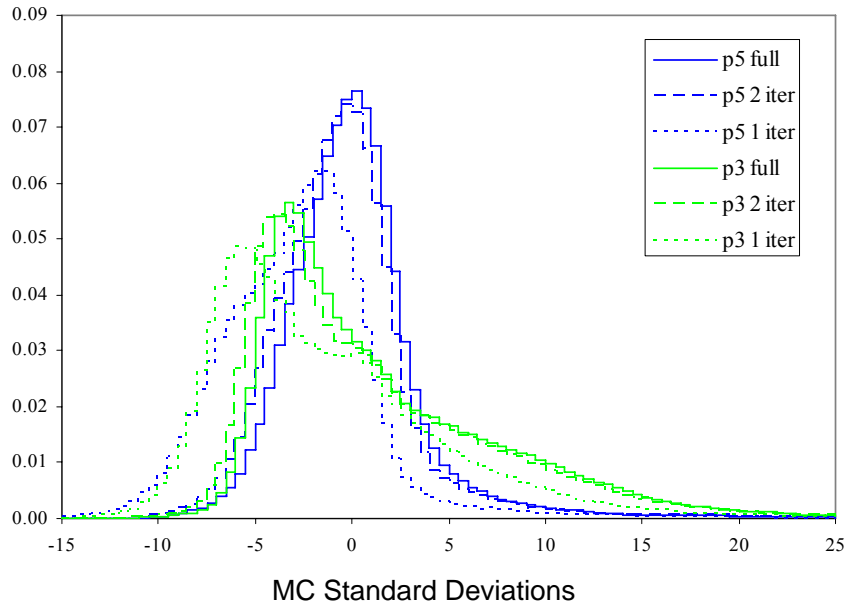


Figure 5. Fractional Frequency Distribution of Voxel Energy Deposited Differences between Discrete Ordinates and Monte Carlo divided by MC Standard Deviation

Finally, sagittal profiles through the CT scan isocenter of the energy deposited obtained from both TORT fully converged calculations are compared with the profile obtained from the EGSnrc calculation in Figure 6. The three profiles were produced by superimposing the transparent colors, blue: 0.1-1%, green: 1-10%, yellow: 10-50%, orange: 50-90%, and red: 90-100% of the maximum value in each profile, onto a black and white CT scan slice of the patient/phantom. However, each profile can be taken as absolute as all three maximums are within 0.5% of one another. Examination of the sagittal profiles again reveals that the use of the P_3 scattering expansion in the discrete ordinates calculations results in a lateral spread in the energy deposited as more photons are scattered out of the beam.

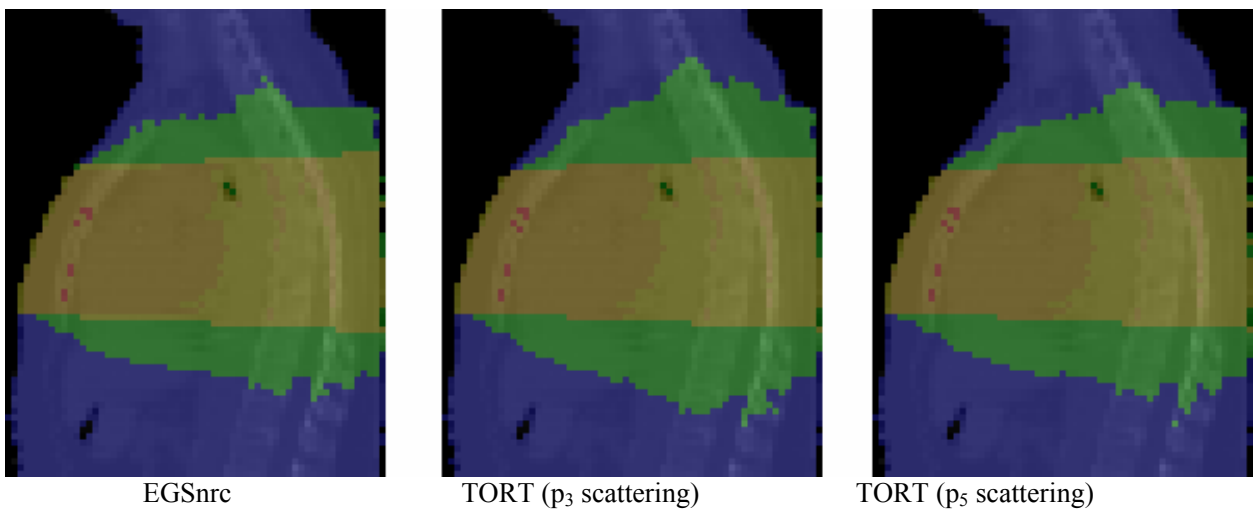


Figure 6. Discrete Ordinates vs Monte Carlo Energy Deposited Sagittal Profiles

The CPU times (using a single AMD 1800+ processor on a LINUX based platform) required for the discrete ordinates and MC calculations are listed in Table 1. Two CPU times are given for the EGSnrc calculations as the total flux and energy deposited results were obtained from different runs. Both times are those required to obtain less than 0.5% uncertainty on the respective quantities in the isocenter voxel. Since this voxel lies in the beam path, very little time is needed to obtain a small uncertainty, as most photons pass through this voxel and contribute to the track length estimate. On the other hand, the energy deposition required a very long running time as it was determined using a collisional estimator. Even though stratified sampling using forced collisions doubled the efficiency over an unbiased run, the MC energy deposition calculation ran more than 50 times longer than the MC flux calculation and almost 10 times longer than the longest discrete ordinates calculation. In addition, short EGSnrc energy deposited runs, with and without electron transport, indicated that four times as much run time is required to get the same statistical uncertainties at the isocenter when electrons are transported.

Table 1. CPU Times Required for Discrete Ordinates and MC Calculations

Code	Calculation	CPU Time (minutes)
EGSnrc	Photon Flux	88
	Energy Deposited	5000
TORT ^a	P ₃ 1 iteration	23
	P ₃ 2 iteration	35
	P ₃ fully converged	185
TORT ^a	P ₅ 1 iteration	62
	P ₅ 2 iteration	97
	P ₅ fully converged	570

^aIncludes GRTUNCL3D CPU times of 5 and 12 minutes for P₃ and P₅ calculations, respectively.

The comparison of the CPU times required to obtain the energy deposited may appear to be unfair from a MC standpoint since one could argue that the MC calculated energy deposition could be obtained by folding kerma factors with the MC calculated flux as was done with the discrete ordinates calculated flux. However, it is a fair comparison as the 5000 minutes represents the actual MC computation time required to produce enough photon collisions to allow statistically meaningful electron transport.

SUMMARY

ANISN and DORT have been used at a number of institutions to optimize material selections for Boron Neutron Capture Therapy (BNCT) filter designs. Both “brute force” optimizations and optimizations using gradient information have been performed. TORT has been used to calculate dose distributions throughout a phantom dog head and throughout a human lower leg. The TORT calculated dose in the dog’s head agreed very well with measured doses. Excellent agreement with Monte Carlo calculated results in the lower leg indicated that deterministic transport codes can produce satisfactory dose mappings for voxel-based anatomical models with significantly less computation cost than Monte Carlo methods. In the photon-only human phantom calculations, the total flux and energy deposited obtained using discrete ordinates compared very well with those obtained using EGSnrc. In addition, the TORT P₅ two iteration calculation produced a distribution very similar to the TORT P₅ fully

converged calculation, again indicating that adequate photon flux distributions can be obtained deterministically with relatively little computational cost.

REFERENCES

1. "DOORS3.1 – One, Two- and Three Dimensional Discrete Ordinates Neutron/Photon Transport Code System," RSIC Code Package CCC-650, Oak Ridge, TN (1996).
2. W. W. Engle, Jr., *ANISN, A One-Dimensional Discrete Ordinates Transport Code with Anisotropic Scattering*, ORGDP Report K-1693, Oak Ridge, TN (1967).
3. W. A. Rhoades and R. L. Childs, "The DORT Two-Dimensional Discrete Ordinates Transport Code," *Nucl. Sci. & Engr.*, **99**, p. 88-89, (1988).
4. W. A. Rhoades, *The TORT Three-Dimensional Discrete Ordinates Neutron/Photon Transport Code*, ORNL Report ORNL/TM-13221, Oak Ridge, TN (1996).
5. D. T. Ingersoll, C. O. Slater, and L. R. Williams, "BNCT Filter Design Studies for the ORNL Tower Shielding Facility," *Trans. Am. Nucl. Soc.*, **75**, p. 28-30, La Grange Park, IL (1996).
6. Y. Karni and E. Greenspan, "Using 'SWAN' for Optimizing the Neutron Source Assembly Design for Boron-Neutron Capture-Therapy Facilities," *Proc. 1st Int. Work. Accel.-Based Neut. Sources for BNCT*, Sept. 11-14, 1994, Jackson Hole, Wyoming, (1994).
7. Y. Karni, E. Greenspan, J. Vujic, and B. Ludewigt, "Optimal Beam-Shaping Assemblies for BNCT Facilities," *Trans. Am. Nucl. Soc.*, **73**, p. 29-30, La Grange Park, IL (1995).
8. E. Greenspan, W. R. Price, and H. Fishman, *SWAN – A Code for the Analysis and Optimization of Fusion Reactor Nucleonic Characteristics*, PPPL Report Matt-1008, Princeton, NJ (1973).
9. D. T. Ingersoll, C. O. Slater, E. I. Redmond II, and R. G. Zamenhof, "Comparison of TORT and MCNP Dose Calculations for BNCT Treatment Planning," *Proc. 7th Int. Symp. on Neutron Capture Therapy for Cancer*, **1**, p. 95-99, Amsterdam, The Netherlands (1997).
10. J. F. Briesmeister, Ed., *MCNP – A General Monte Carlo N-Particle Transport Code*, LANL Report LA-12625-M, Los Alamos, NM (1993).
11. F. J. Wheeler and D. W. Nigg, "Three-Dimensional Radiation Dose Distribution Analysis for Boron Neutron Capture Therapy," *Nucl. Sci. & Engr.*, **110**, p. 16-31 (1992).
12. I. Kawrakow, "Accurate Condensed History Monte Carlo Simulation of Electron Transport. I. EGSnrc, the new EGS4 version," *Med. Phys.* **27**, 485 (2000).
13. J. E. White, *et. al.*, "VITAMIN-B6: A Fine-Group Cross Section Library Based on ENDF/B-VI for Radiation Transport Applications," *Proc. Int. Conf. Nucl. Data Sci. & Tech.* Gatlinburg, TN (1994).
14. R. A. Lillie, "GRTUNCL3D: A Discontinuous Mesh 3-D First Collision Source Code," *Proc. Am. Nucl. Soc. RP&S Div. Top. Conf.*, Nashville, TN (1998).

MCNP / MCNPX OVERVIEW FROM A MEDICAL PHYSICS PERSPECTIVE

Tim Goorley
MCNP Team, X-3
Los Alamos National Laboratory

Abstract³

The Monte Carlo computer codes MCNPTM and MCNPXTM, developed at Los Alamos National Laboratory, are used for a wide variety of medical physics calculations. They have the ability to simulate coupled photons, electrons, positrons, protons and neutrons through general purpose 3-D geometries, with high quality data (or models where data is not available), to calculate particle flux, current, energy deposition, or reaction rates. The robust benchmarking and validation efforts and the thousands of users world wide make MCNP(X) one of the most trusted radiation transport codes in the world. This document briefly discusses the MCNP(X) capabilities and issues currently of interest to medical physics calculations.

Transport Capabilities

MCNP and MCNPX have the capability to transport a variety of particles over a large range of energies, but typical medical physics calculations employ electrons, photons and protons. The physics interaction models and data in the code are valid for electrons and positrons from 1 keV to 1 GeV. Improved electron physics in the newest release of MCNP5 (version 5.1.40) can be used by setting the 18th entry on the DBCN card to 2. Photons can be tracked from 1 keV to 100 GeV. MCNPX and MCNP6⁴ can transport protons, mesons, pions, and other high energy particles from ~1 GeV to 100s of GeV and above. MCNPX can transport these particles down to a few MeV.

Geometry Modeling Capabilities

MCNP(X) has the ability to represent a variety of surfaces which can be combined to enclose unique volumes of three dimensional space. Each independent region of space is called a cell, and can have its own material and density. The combination of planes, ellipsoids, cones and user-defined surfaces have been used to construct “analytical” phantoms. Special features allow for the duplication, translation and rotation of cells to save user setup time. Additionally, MCNP(X) contains the ability to represent a lattice, a regular replication of hexahedra or hexagonal prisms. A lattice geometry of cubes is frequently used to represent CT data within MCNP(X). With appropriate image segmentation capabilities (i.e. thresholding), each CT pixel or group of pixels from the original image can be represented as an individual voxel in the MCNP(X) lattice geometry with a single homogenized material. For greater accuracy in their calculation, users may increase the voxel based geometry's resolution (smaller individual voxels) and range (more total voxels) to the memory limits of the computing hardware. Larger lattices, however, can greatly increase MCNP(X) runtimes.

³ This document is a Los Alamos National Laboratory technical release, LA-UR-06-2393

⁴ MCNP6 is a developmental code not currently released outside LANL.

MCNP5 now offers a free database of analytical and voxel based medical physics phantoms with the RSICC distribution, and the web: <http://cmpwg.ans.org/phantoms.html> MCNP(X) input decks for two analytical whole-body and two highly detailed voxel models of the head and male pelvis are included. The MCNP5 efforts in the European Union's medical physics code intercomparison (QUADOS) are included in this database. Voluntary donations of phantom input decks are welcome and appreciated.

Tally Capabilities

A powerful resource within MCNP(X) is the ability to calculate a wide variety of quantities. Particle fluxes, reaction rates, energy deposition, charge or detector pulse collection, and radiographs are frequently used in medical physics calculations. These quantities can be calculated over surfaces, cells, or user defined grids (mesh tallies) placed independently of the geometry. Parallel calculation ability and a wide variety of variance reduction techniques exist to help users reduce total computational time.

Neglected Existing Capabilities

There are several features in MCNP which are available to the medical physics community which are not being used to their potential, at least in reported literature. The ability to do time dependant sources and tallies, for example could be used to simulate the progress of an ingested radioisotope through the human body, and tally time dependant organ doses. The new randomized (stochastic) geometry could possibly be used to represent biological or anatomical features such as cortical bone or alveoli in the lung. Some users also find that it is useful to force particle collisions with particular elements with the PIKMT card, most frequently to create prompt capture gammas from neutron absorption. This might allow users to calculate photon dose from a neutron source with less computational effort.

Medical Physics Issues

The medical physics community has voiced a number of desirable features to the MCNP developers. These features range from simple user interface issues, such as long file names, shorter output files, a materials library, and html output, to adding significant new features. Many users want the ability to directly import DICOM or other CT data into MCNP, which includes improving MCNP memory management of lattices. Some users want the ability to easily specify pre-defined radioisotope source, such as Tc-99m or Co-60, as well as the decay emissions of their daughter products. Others want MCNP to be able to handle calculations on the micron or nanometer levels, to calculate dose to cellular structures or even DNA. Another common request is for an adjoint capability to speed up calculations. The MCNP developers are always interested in hearing these requests to make the code more useful to its users.

Availability

MCNP5, MCNPX and their corresponding nuclear data are available on 1 DVD through the Radiation Safety Information Computational Center (<http://www-rsicc.ornl.gov/>).

Medical Physics Primer

A medical physics primer, which will step new MCNP users through representative medical physics calculations, is being written. This primer will include discussions of different sources and tallies, and use voxel and analytical whole body phantoms from the database. This resource will be available on the MCNP website when it is completed.

PENTRAN CODE SYSTEM

Glenn Sjoden and Ali Haghight
University of Florida

The linear Boltzmann transport equation describes the behavior of neutral particles in terms of spatial, angular, and energy domains as they interact in a system; the steady state fixed source form of the transport equation (forward) is given, using standard notation:

****(III.A.2.1)

$$\hat{\Omega} \cdot \nabla \psi(\vec{r}, \hat{\Omega}, E) + \sigma(\vec{r}, E) \psi(\vec{r}, \hat{\Omega}, E) = \int_{\forall E' 4\pi} \int dE' d\Omega' \sigma_s(\vec{r}, \hat{\Omega}' \cdot \hat{\Omega}, E' \rightarrow E) \psi(\vec{r}, \hat{\Omega}', E') + q(\vec{r}, \hat{\Omega}, E)$$

The left side of Equation (III.A.2.1) represents streaming and collision terms (loss), and the right side represents scattering and fixed source terms (gain). Discrete ordinates approximations of the linear Boltzmann equation invoke a discretization of the space, angle, and energy variables to model neutral particles in a system. Discretization of the energy variable is accomplished by spectrally averaging over a few to several energy groups ($g=1, G$), spanning from high to low particle energies. In steady state with fixed group sources, this results in the forward multi-group form of the transport equation operating on the forward group angular flux ψ_g :

(III.A.2.2)

$$\hat{\Omega} \cdot \nabla \psi_g(\vec{r}, \hat{\Omega}) + \sigma_g(\vec{r}) \psi_g(\vec{r}, \hat{\Omega}) = \sum_{g'=1}^G \int_{4\pi} d\Omega' \sigma_{s_{g' \rightarrow g}}(\vec{r}, \hat{\Omega}' \cdot \hat{\Omega}) \psi_g(\vec{r}, \hat{\Omega}') + q_g(\vec{r}, \hat{\Omega})$$

The PENTRAN (Parallel Environment Neutral-particle TRANsport) code system is actually a suite of codes that allow one to readily generate and solve 3-D Boltzmann transport models and gather parallel data. The computational model (the material spatial grid) can be generated using PENMSH, a mesh generator for 3-D Cartesian geometries. Another code that processes the PENMSH output, called PENINP, automatically generates a 3-D input deck ready for processing in PENTRAN, including an automated fixed source linear projection of the source distribution. PENMSH renders x-y slices through selected z-levels for visual 3-D geometry verification. Other tools for 3-D visualization are in development. The transport code itself is PENTRAN, which is described in more detail below. The complexities of parallel memory in PENTRAN (due to the localized memory on each processor) require a post processor to gather parallel data for the user. Post processing of parallel data stored in multiple files is performed by PENDATA to seamlessly gather parallel results for the user. 3-D interpolation of results can be accomplished using one of two available tools (PENPRL or 3DI).

PENTRAN is a multi-group, anisotropic discrete ordinates code for 3-D Cartesian geometries specifically designed to solve the linear Boltzmann equation on distributed memory, scalable parallel computer architectures. PENTRAN was written from scratch in 1995 in FORTRAN for parallel computing architectures via the MPI (Message Passing Interface) library, and has

undergone 10 years of development and testing, with applications in shielding, nuclear detection, reactor physics, and medical physics. A variety of domain decomposition alternatives can be specified in PENTRAN by the user for automatic distribution and subsequent iterative solution on a distributed parallel computer. Specifically, solution of a transport problem can be rendered using automatic domain decomposition among the angular, energy, and spatial variables, including any desired hybrid decompositions among all three domains. PENTRAN has been tested extensively, and has been used to accurately compute neutral particle flux solutions for a variety of test problems. It has compared well with traditional codes, and has also rendered solutions in excellent agreement with experimental data. The following problems have been successfully modeled and tested against experiment or Monte Carlo calculations over the past 10 years:

- OECD/NEA Venus-3 3-D PWR Benchmark
- OECD/NEA Kobayashi Benchmarks
- ISFSI Fuel Storage Cask
- Prompt g-Neutron Activation Analysis (PGNAA) device
- BWR Reactor Simulation
- He-3 Detector System
- X-Ray Room Simulation*
- CT-Scan Simulation*
- HEU Criticality Benchmark
- QUADOS Brachytherapy Problem Model*
- OECD/NEA MOX 2-D & 3-D Benchmarks
- WG-Pu/U Homeland Security Detection problem (in development)
- Gamma ray IMRT simulation*
- UFTR Beam port Model

*=medical physics problem

In addition to parallel execution, key PENTRAN features important for 3-D deterministic medical physics applications include:

- (i) Tunable Angular Dependent Sources. Sources in PENTRAN can be defined on a per angle basis, enabling precise modeling of any particular beamlet in a medical physics therapy model, as required
- (ii) Adaptive Differencing with Block-AMR. An adaptive differencing strategy developed in PENTRAN provides for the possibility of directing the code to automatically change the spatial differencing scheme to adapt to problem physics and applied discretization within each energy group. The current version of PENTRAN includes the linear diamond-zero (DZ), the Directional Theta Weighted (DTW), and the Exponential Directional Weighted (EDW) spatial differencing schemes. This is important with a Block-Adaptive Mesh Refinement (AMR) where various 3-D grid densities are mixed throughout a problem (leading to different mean free paths), since the differencing scheme must adapt to localized mesh strides and scattering physics.
- (iii) Arbitrary built-in Sn quadrature and Pn scattering expansion orders. 3-D Sn Quadrature sets are built-in and readily user selectable for arbitrary order Legendre-Chebyshev (limited only by memory) or Level Symmetric through S20 (limited by positive weight). Pn order is not limited if cross sections are

available. This is important to medical physics calculations, since medical physics simulations typically require an order of magnitude more in discrete ordinates dimension than reactor physics simulations.

- (iv) Ordinate Splitting (OS). This is a feature that permits readily selectable angular refinement in a direction of interest, most notably where ray effects may be expected. Use of OS has demonstrated high accuracy without complete refinement of angles on the unit sphere. A single ordinate can be split using equal-weight quadratures up to arbitrary order (limited by memory). Again, this can be vitally important to enable accurate medical physics simulation; if a beamlet problem is being modeled, OS in the direction of the beamlet should be performed, directly selectable in PENTRAN.
- (v) Two-Level Optimized Parallel Memory. All memory in PENTRAN is parallelized in data structure; each parallel node only stores the portion of the problem phase space that it actually works on, permitting parallel scalability with problem size. Therefore, larger problems can be solved by adding processors. Also, memory on each node is optimized in a “large memory/small memory” coarse mesh structure to automatically minimize phase space storage for the problem being solved.
- (vi) Detailed flux, current, and particle balance information. Detailed information, including 3-D fluxes, partial currents, Legendre moments, coarse mesh balance tables, angular fluxes, etc are available, which can be highly valuable in analysis of surface effects, dosimetry, and solution verification. There are numerous options available in PENTRAN.

Many near-term specific needs remain for deterministic medical physics modeling and simulation efforts; future issues necessary for effective modeling and simulation of deterministic medical physics problems include: establishment of photon cross sections, establishment of code links to DICOM Computed Tomography image data, development of methodologies to treat secondary electron dose effects in deterministic simulations, and development of rapid acceleration of deterministic computations.

- Cross Sections. Cross sections are typically not an issue for Monte Carlo codes, which have direct data links to point-wise photonuclear/photoatomic cross sections. However, due to the multigroup nature of cross sections for deterministic models, there is an essential need for standardized photon cross section libraries with energy group bins specifically tailored for specific medical physics purposes, e.g. libraries for linear accelerators, Co-60 therapy, diagnostic X-ray imaging, CT Scanning, etc. Standardization of and ready access to validated, benchmarked cross section libraries (benchmarking using Monte Carlo computations) would expand the potential user base for deterministic medical physics modeling and simulation, permitting both deterministic and Monte Carlo methods to be used in concert to achieve minimization of dose, optimization of treatment plans, minimization of facility costs, etc.

- Digital Patient Image Data. Most medical physics methods now incorporate some form of digital image of the patient (often using Computed Tomography scans) to effectively yield 3-D position and tissue density information. Currently, the DICOM image standard is used to store this (with other data), and deterministic (and Monte Carlo) codes must be able to interface with this image format in order to be able to link to patient data.

- Secondary Electron Effects and Sn Acceleration. High energy photons, particularly in linear accelerator applications, give rise to secondary electrons that cause non-trivial doses at tissue sites distal to the delivery site; therefore, provisions for treatment of electron transport physics must be accounted for in deterministic codes. This is problematic for deterministic computations, given that direct deterministic solution of electron transport leads to a non-linear form of the Boltzmann equation coupled with Maxwell's Equations. Also, the mean free paths for electrons can be several orders of magnitude shorter in tissue relative to the mean free paths of the original photons causing them, leading to extremely difficult convergence issues for differencing schemes in deterministic solutions. Also, due to the inherent nature of medical physics problems, with high levels of streaming and non-linear behavior of the angular flux, traditional synthetic diffusion acceleration methods that may work well in reactor physics problems are not effective for medical physics problems; new acceleration methods must be implemented. In the case of both electron transport and acceleration methods, deterministic adjoint methods and other research is underway to address these problems.

At the University of Florida, we are focusing on each of these problems to directly generate solutions to difficult computational medical physics applications in real world problems.

COARSE MESH RADIATION TRANSPORT CODE COMET: RADIATION THERAPY APPLICATION

Farzad Rahnama, Megan Satterfield and Dingkang Zhang, Nuclear and Radiological Engineering and Medical Physics Programs,
George W. Woodruff School
Georgia Institute of Technology

COMET Method

The main objective of this research has been to develop an accurate 3-D particle transport method, which is now termed COMET. Heterogeneities within the coarse mesh and the geometry of the problem are completely retained without any homogenization. COMET also contains an accurate and self-consistent global dose reconstruction procedure.

The methodology is begun with the transport equation and any boundary condition.

$$\begin{aligned} \hat{\Omega} \cdot \nabla \psi(\vec{r}, \hat{\Omega}, E) + \sigma_t(\vec{r}, E) \psi(\vec{r}, \hat{\Omega}, E) \\ = Q(\vec{r}, \hat{\Omega}, E) + \int_0^\infty dE' \int_{4\pi} d\hat{\Omega}' \sigma_s(\vec{r}, \hat{\Omega}', E' \rightarrow \hat{\Omega}, E) \psi(\vec{r}, \hat{\Omega}', E') \end{aligned} \quad (1)$$

$$\psi(\vec{r}_b, \hat{\Omega}, E) = B \psi(\vec{r}_b, \hat{\Omega}, E), \quad \vec{n} \cdot \hat{\Omega} < 0, \quad \vec{n} \cdot \hat{\Omega}' > 0, \quad \vec{r}_b \in \partial V \quad (2)$$

The usual notation is used in the above equation (B is the boundary condition operator including vacuum and reflective conditions). The global problem is then decomposed into a set of local fixed source problems over user-specified non-overlapping coarse meshes, V_i .

$$H \psi_i(\vec{r}, \hat{\Omega}, E) = Q_i(\vec{r}, \hat{\Omega}, E) \quad (3)$$

$$\psi_i^-(\vec{r}_{ij}, \hat{\Omega}, E) = \psi_j^+(\vec{r}_{ij}, \hat{\Omega}, E) \quad \vec{r}_{ij} \in \{V_i \cap V_j\} \quad \text{for all } V_j \text{ bounding } V_i \quad (4)$$

Here H is the transport operator of equation (1). We note that the solution of equations (3) and (4) are the same as that to equations (1) and (2) provided that boundary/interface condition (4) is found from equations (1) and (2). The unknown boundary condition (4) is approximated in COMET by a truncated expansion of the response functions which are solutions to the equations below:

$$\begin{aligned} HR_{is}^m(w_i) = Q(w_i) \\ \text{with } R_{is}^m(w_{is}^-) = \begin{cases} \Gamma^m(w_{is}^-), & \text{for } \vec{r} \in \partial V_{is} \\ 0, & \text{otherwise} \end{cases} \end{aligned}$$

Where, Γ is the m^{th} member of a set of functions orthogonal on the half space. Examples include both discrete and continuous Legendre polynomials. From this, a library is generated with precomputed response functions. In radiation therapy applications, these will be a function of the material density or rather the CT index number. In order to obtain a dose distribution within a defined geometry, the user defines the mesh grid for the problem. The response functions are then accessed via the precomputed library. Last, a sweeping method

is then used to couple the meshes through their mesh interface angular fluxes or currents to converge on the dose distribution in the system.

Simple Benchmark Problems

A simple homogeneous problem was used initially to test COMET's application to radiation therapy. The geometry was defined as a 20 cm x 30 cm region of water. It was separated into 150 regions with each mesh being 2 cm x 2 cm. The photons impinged normally on the 30 cm side of the phantom with an initial energy of 4-5 MeV. For simplicity, it is assumed that secondary electrons deposit their energy locally. In EGS to obtain an uncertainty of less than 0.3 %, 160 million particles were tracked. This required 3700 seconds. When comparing COMET to the EGS reference solution, an average relative error and maximum relative error of 1% and 2% respectively were obtained. The COMET calculation only required 122 seconds.

A second simple benchmark problem has also been tested. The size of the entire geometry and each coarse mesh remain the same as before. Each coarse mesh is still homogeneous; however, now the meshes can contain one of three different materials – bone, air, or lung tissue. Again, the photons impinge normally with energy of 4 – 5 MeV, and secondary electron energy is deposited locally. In this case, the EGS reference solution required 2 billion particles to obtain an uncertainty less than 1.4%. The time to run this case was 47,800 seconds. In comparison to the reference solution, the average relative error was 1.2%, while the maximum relative error was 2.4%. As before, the time required was only 122 seconds.

Future Benchmark Problems

There are three benchmark problems that will be solved using COMET, and these results will be compared to experimental dose deposition values obtained at Emory clinics. A comparison will be made between the COMET solution from a 3D homogeneous water phantom and the experimental values. A simple slab benchmark composed of water, aluminum, and lung tissue will also be solved using COMET and compared to the experimental results. Also, a CT dataset of an anthropomorphic phantom will be used to obtain a coarse-mesh solution. The same anthropomorphic phantom will be irradiated in order to obtain experimental values of dose deposition.

Conclusions

The COMET method does provide very accurate results for photon transport in both homogeneous and heterogeneous media. The results that have been obtained are comparable to those calculated using continuous energy Monte Carlo method. This method has shown to be substantially faster than both fine mesh deterministic transport and Monte Carlo methods. In the future, more numerical and experimental benchmark problems will be created. It is also quite important that coupled photon, electron, and neutron transport be implemented in the radiation therapy applications. The COMET method will also be extended to three dimensions, and improved sweep techniques are anticipated.

MINERVA: A MULTIMODALITY PLUGIN-BASED RADIATION THERAPY TREATMENT PLANNING SYSTEM

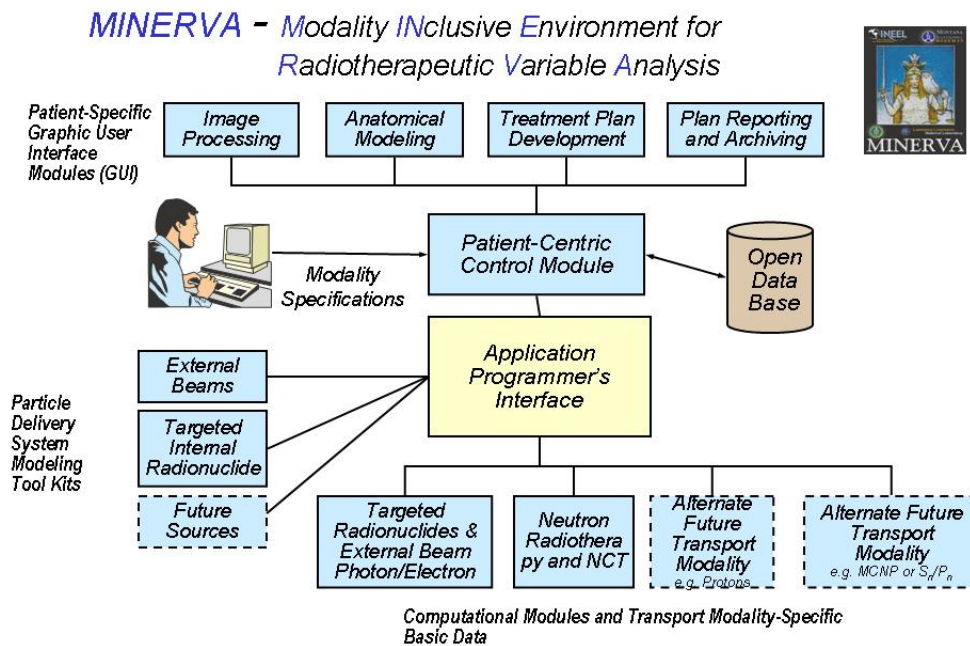
Dave Nigg
Idaho National Laboratory

INTRODUCTION

MINERVA is a patient-centric, multi-modal, radiation treatment planning system (RTPS) that can be used for planning and analyzing several radiotherapy modalities, either singly or combined, using common modality independent image and geometry construction and dose reporting and guiding. This system builds upon experience accumulated at the Idaho National Engineering and Environmental Laboratory (INEEL), Montana State University (MSU), and Lawrence Livermore National Laboratory (LLNL). MINERVA is being developed with the Java¹ programming language for interoperability. MINERVA employs an integrated plugin architecture to accommodate multi-modal treatment planning using standard interface components. The MINERVA design also facilitates the future integration of improved planning technologies.

CODE DESCRIPTION

The capabilities of the various modules that have been developed for the MINERVA system, shown as the solid outlined boxes in Figure 1, are described in this section.



Patient Module

The Patient module is the focal point of MINERVA. It manages the entire treatment planning process, launches and monitors the Image, Model, and Analyze modules, and

provides communication with the patient database. The user interface allows entry of general information about the patient (name, contact information, etc.), as well as physician data and treatment history.

A complete XML file specification of all of the information contained in the database and a set of XML-based import/export tools have been developed. This same XML file specification will also be used to help define the API between MINERVA and the modality-specific transport modules.

Image Module

The Image module prepares and processes the images for use by the Model module. The Image module currently supports DICOM-RT, QSH, JPEG, and raw image importation. Standard image processing features, including noise filtering, gamma correction, and contrast enhancement, are also provided. Full plugin support was added so that image import formats, image manipulation operations and image import filters can be added later.

A rigid registration system based on maximization of mutual information² has been included. A reslicing tool, which performs a pixel-by-pixel interpolation between existing image slices to create a uniform slice spacing, has been developed to facilitate the registration.

Model Module

The Model module creates the anatomical geometry of the patient and target based on the image data received from the Image module. Anatomical structures are defined by various methods, and materials are assigned to these regions. Several methods are provided for manually or semi-automatically defining regions of interest (ROIs) from multi-modal image sets. All modeling can be conducted with multiple image sets along the three principal orthogonal axes simultaneously and interchangeably. Multiple image sets may be used simultaneously to define the ROIs.

Analyze Module

Control of the planning and dose reporting functions is consolidated in the Analyze module. The planning function controls the launching of the source and transport plugins, which perform the actual dose calculations. Results from these plugin modules are saved to the database. The dose reporting function accesses the database to read the dose information for each field in the plan, and performs the weighted dose combination using modality-dependent biological weighting factors (RBE) by field, region, and dose component. Binary agents may also be included, with accumulation factors that may vary by region and compound type. Dose reporting functions include display of isodose contours, dose volume histograms, and dose depth data.

MTR Source Module

The molecular targeted radiotherapy (MTR) source module is a plugin launched from the Analyze module to calculate the activity map for a targeted radionuclide treatment plan. Activity map generation is presently implemented in two modes - manual assignment of a constant value to a region, and back projected calculation of the average region activity from a radiographic image.

MTR Transport Plugin

The computation engine for the MTR radiation transport calculation is the PEREGRINE³ code. The PEREGRINE code is a coupled photon-electron Monte Carlo transport code which was initially designed to compute dose distributions from external beam radiotherapy simulations. The capability to perform transport calculations based on an internal source has been added and tested,⁴ and a Java-based interface has been designed to allow PEREGRINE to work as a plugin for the MINERVA system.

Neutron Transport Plugin

The neutron transport module is the computation engine for external beam neutron therapy modalities (BNCT, fast neutron therapy, etc.) and internal localized and distributed neutron sources (e.g. ²⁵²Cf). A coupled neutron-photon calculation is performed, using the univel geometry.⁵ Continuous energy cross section data from the latest Evaluated Nuclear Data File (ENDF) are used, with a detailed photon production model. The photon transport calculation assumes charged particle equilibrium. Explicit tracking of electrons produced by photon interactions is generally unnecessary for this particular application, as opposed to the case for external beam photon therapy.

STATUS AND FUTURE WORK

The common RTPS modules (Patient, Image, Model, and Analyze) are functionally complete. A full computation path, with data communication through an application programmers interface (API) as shown in Figure 1, has been established for MTR treatment planning, including the associated transport plugin.

Although the primary emphasis in the near term is on MTR applications, transport and source plugins will ultimately be created for additional treatment modalities, including neutron-based therapies, brachytherapy, external beam proton radiotherapy, and external beam photon and electron radiotherapy. The interfaces for the common RTPS modules will be refined in response to feedback from clinical test facilities.

ACKNOWLEDGEMENTS

This work was sponsored by the United States Department of Energy, Office of Science, under DOE Idaho Operations Office Contract DE-AC07-99ID13727 and University of California Lawrence Livermore National Laboratory under contract W-7405-Eng-48.

REFERENCES

1. Gosling J, Joy B, Steele G, *The Java Language Specification*, Addison-Wesley (1996).
2. Viola P and Wells WM, *Int J Comp Vis* **24**(2) 137-154 (1997).
3. Hartmann-Siantar CL, et al., *Med Phys* **28** 1322-37 (2001).
4. Descalle M-A, Hartmann-Siantar CL, Dauffy L, Nigg DW, Wemple CA, Yuan A, DeNardo GL, *Canc Biother Radiopharm*, **18**(1) 71-80 (2003).
5. Frandsen MW, Wessol DE, Wheeler FJ, Starkey D, *Rapid geometry interrogation for uniform volume element-based BNCT Monte Carlo particle transport simulation*. Proceedings of the Eighth International Symposium on Neutron Capture Therapy, September 13-18, 1998, La Jolla, CA, USA, Plenum Press, New York.

TRANSMED: DETERMINISTIC PHOTON TRANSPORT FOR EXTERNAL BEAM THERAPY

Erno Sajo* and Mark L. Williams[†]

*Louisiana State University, Department of Physics

[†]Oak Ridge National Laboratory

INTRODUCTION

The last decade has seen unprecedented advances in the technology of radiation therapy. New modalities have appeared, such as intensity modulated and conformal therapies, which permit radiation delivery to a complex three-dimensional (3D) volume with optimized distribution of dose. Thus, in principle, the dose can now be escalated to the tumor while minimally affecting the surrounding normal structures. Consequently, a large dose gradient is often generated at the interface of neoplastic and normal tissues, where small spatial deviation from the optimal dose distribution can be detrimental to the outcome of the treatment. Hence, in order that the new modalities could be realized to their full potential, accurate and precise treatment planning has become imperative. To meet this objective, aided by high-performance computing, advanced calculational methods are now being considered. Monte Carlo (MC) methods have received thus far the most attention due to their extensive modeling capability in irregular 3D geometry. Although currently not used in clinical patient therapy planning, customized MC codes are proposed for this role^{1,2}. However, detailed dose contours require a large number of tally sites and statistical uncertainties, inherent in the MC method, make dose optimization difficult. Thus, long running times are usually required to obtain the desired accuracy.

Deterministic methods of solving the Boltzmann transport equation are an alternative to MC methods for many problems. This approach is often superior for problems involving significant attenuation and events that are “unlikely” in the Monte Carlo sense. In addition, this solution provides the full phase-space in one run, giving a detailed space-energy-directional distribution of the radiation field, which is well suited for optimization studies where high resolution of dose contours are needed. However, until recently, the geometrical modeling capability of deterministic methods was limited. Because patient anatomy and the components of the radiation delivery system are spatially complex, deterministic methods have not been practical. In addition, the conventional numerical method for solving the transport equation, the discrete ordinates approach, generates numerical artifacts, known as ray effects, in low-density media³.

Recently, deterministic approaches using the method of characteristics (MOC) have been developed. The advantage of the MOC is that it is capable to treat geometries composed of arbitrarily shaped objects^{4,5}. This work outlines the application of a 3D MOC code, TransMED, to compute dose distributions for external beam therapy. TransMED utilizes combinatorial geometry routines similar to those in the MARS package originally developed for MC codes⁶. This allows a complex system, – such as a medical accelerator with various beam shaping devices, and patient anatomy obtained from imaging studies – to be modeled realistically. TransMED is based on the code TransFX, which is a reactor analysis software developed by TWE corporation for neutron and photon transport calculations⁷. A modified

version of TransMED is described in this paper, which includes several routines developed at the Nuclear Science Center of Louisiana State University (LSU) to enhance its capability to therapy applications, as well as external modules that interface with the transport computations. These include improved computations using analytical expressions for transport of uncollided flux, a special approach to treat scattering from the accelerator components, generation of comprehensive photon interaction data library optimized for therapy applications, a module for computations of X-ray source emission spectra in medical accelerator targets, a routine to generate realistic 3D models of accelerator components, and routines to generate 3D models of patient anatomy from imaging studies compliant with the DICOM standard.

Results are presented for the kerma distribution in a water phantom exposed to X-rays generated by a medical accelerator, and are compared to MC predictions. The current version of TransMED is limited to the computation of kerma rather than the absorbed dose because

of its lack of electron transport capabilities. Kerma and absorbed dose responses differ in regions where charge particle disequilibrium exists, such as interfaces of bone-tissue or tissue-lung. In these regions corrections for secondary electron transport may be important.

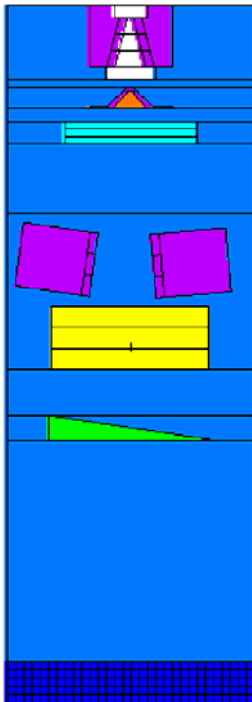


Figure 1. Model of accelerator head geometry.

MATERIALS AND METHODS

The spatial domain of the computations is divided into two regions: \mathcal{R}_A corresponds to the accelerator gantry region, and \mathcal{R}_P is the patient or phantom volume of interest. Each region contains a number of objects or bodies of uniform composition. In the accelerator region, the bodies represent accelerator components (or subdivisions thereof) such as the linear accelerator (LINAC) target, primary collimator, flattening filter, and jaws, as well as multi-leaf collimators, blocks, or other field shaping devices. In the patient region the bodies usually correspond to rectangular voxel elements describing a phantom or patient anatomy, such as contained in CT image files. Figure 1 illustrates a typical model for which the transport calculations would be performed in therapy applications.

The CEPXS/ONEDANT codes are used in our present computational system to compute the X-ray source spectra for medical LINAC targets, since these can be modeled as 1D slabs with an incident electron beam⁸. The CEPXS⁹ code generates coupled photon-electron multi-group data for use in the one-dimensional discrete-ordinates code ONEDANT¹⁰. The computed photon leakage spectrum at the target is subsequently input to TransMED for 3D transport calculations of the LINAC head configurations, such as shown in Figure 1.

In the description of the flux density, the concept of collision flux is used: the angular flux can be expressed as the sum of various collision fluxes, corresponding to how many previous collisions the particles experienced. The uncollided flux throughout the system is due to photons emitted directly from the LINAC target. The collided flux density consists of secondary photons generated by various types of reactions both in the accelerator and the

patient. In computing the collision fluxes, the assumptions are made that (1) the angular flux density in region \mathfrak{R}_A is not significantly affected by the collision fluxes from the patient volume. Thus the collided flux density incident on the patient is exclusively due to collisions in the accelerator. (2) The angular flux in the patient region is not significantly affected by collision fluxes higher than the first order from the accelerator volume. This is because the patient dose is mainly due to the uncollided photons in the primary beam and secondary interactions inside the patient. A relatively small fraction of the dose is due to scattered photons originating in the accelerator head. The dose contribution of photons coming from region \mathfrak{R}_A and experiencing more than a single collision is small due to energy degradation and attenuation. The higher order collision fluxes due to scattering in the patient are, however, included in the dose calculations.

Detailed description of the computational method employed by TransMED-LSU, including the discretization of direction and energy, the analytical and numerical calculations of the uncollided flux and those of the collision sources, and the implementation of the method of characteristics are discussed by Williams et al¹¹. Here only a brief review of the computational flow is provided: The first-collision sources in the accelerator region, generated by the primary photon source at the target, are first calculated for the LINAC head components shown in Figure 1. Most of the bodies in the LINAC head model include multiple scatter-points to better represent the scatter source distribution. The primary photon source also produces an uncollided flux density and first-collision source in the phantom region of Figure 1, which are computed directly from analytical expressions, as shown by Williams et al¹¹. Next, the first-collision sources obtained for the bodies in the LINAC head model are used to compute second-collision sources for the rectangular bodies of the phantom region. Finally TransMED solves the Boltzmann equation with the first- and second-collision sources to compute the collided flux density and the kerma values for all bodies in the phantom region.

RESULTS

Example calculations were performed to compare deterministic results to Monte Carlo values for the kerma distribution within a homogeneous $30 \times 30 \times 15 \text{ cm}^3$ water phantom exposed to LINAC x-ray sources at a source-to-surface distance (SSD) of 80 cm. Fig. 1 shows a central axis cross sectional view of the problem geometry. An auxiliary program has been developed to easily produce the appropriate 3D combinatorial geometry input for describing the LINAC head with specified settings for the secondary collimator jaws. The “beam modifiers” component of the accelerator region shown as a wedge in Fig. 1 is not considered for open field calculations. The reference case for this study corresponds to $14 \times 14 \text{ cm}$ open field, with a 10 MV photon source spectrum produced by 10 MeV electrons incident on a 5 mm thick tungsten target (the “10MV/5mm-W” source). The LINAC target is treated as a point source located at the origin of the coordinate system.

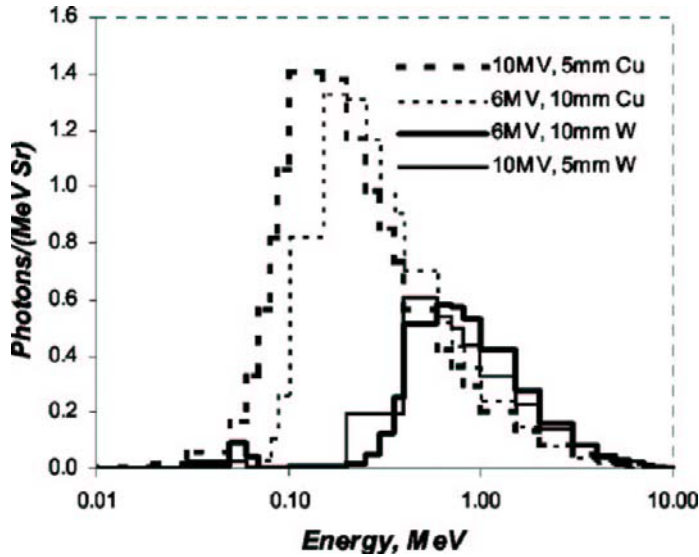


Figure 2. LINAC target source spectra

Additional calculations were performed for three other LINAC target sources – equivalent to 6 and 10 MV x-rays, produced by 5 and 10 mm thick targets of either copper or tungsten – to test the accuracy of the deterministic program for treating variations in source energy spectra. These sources are denoted respectively as “10MV/5mm-Cu”, “6MV/10mm-Cu”, and “6MV/10mm-W” in the inset of Fig. 2. The energy spectra for the four sources used in our analysis are shown in Figure 2, normalized to 1 photon/second. These were computed using a deterministic, one dimensional,

coupled electron-photon transport calculation as described in an earlier study⁽⁸⁾. In all cases the angular distribution of the LINAC target source is assumed uniform in the solid angle from 0 to 14 degrees from normal, and is equal to zero outside of this solid angle. Although the angular distribution of an actual LINAC source is forward-peaked along the normal axis, it was not deemed necessary to utilize the more realistic shape for this purely numerical study. Another variation of the reference case included a wedge attenuator to produce a transverse gradient in the field. Finally, a case was run to compute the kerma distribution in the phantom with the LINAC jaws set to generate a 6x6 cm² beam, in order to examine the accuracy of the deterministic calculations for smaller field sizes.

Each of the above cases were calculated using the TransMED-LSU deterministic code and the MCNP (version 4C2) Monte Carlo code developed by Los Alamos National Laboratory.⁽¹²⁾ The Monte Carlo photon transport calculations were run initially with approximately 10⁸ histories and tallied kerma values using a tracklength estimator with a water-kerma response function – the same as utilized in the deterministic computations. However, even with this large number of histories, the Monte Carlo results in some locations outside of the beam had excessive statistical uncertainties. A next-event-estimator also was used to tally kerma values at selected locations. The execution time per history is considerably greater with this type of tally, but improved statistical uncertainty often can be obtained with fewer histories. Unfortunately the next-event-estimator in MCNP-4C2 used in this study is limited to only twenty response tallies per run; hence it was used mainly to confirm the tracklength estimator results.

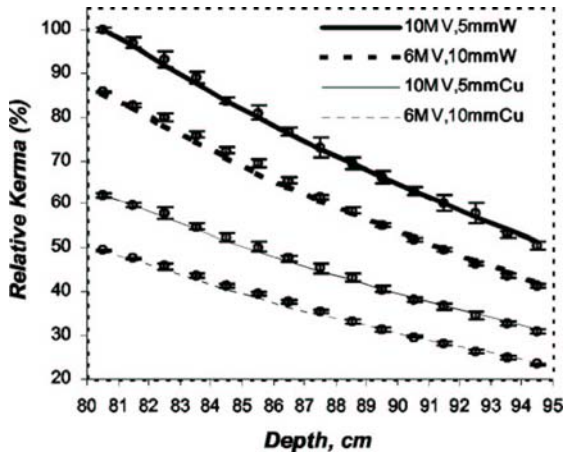


Fig. 3. Deterministic vs MC kerma depth-dose profiles.

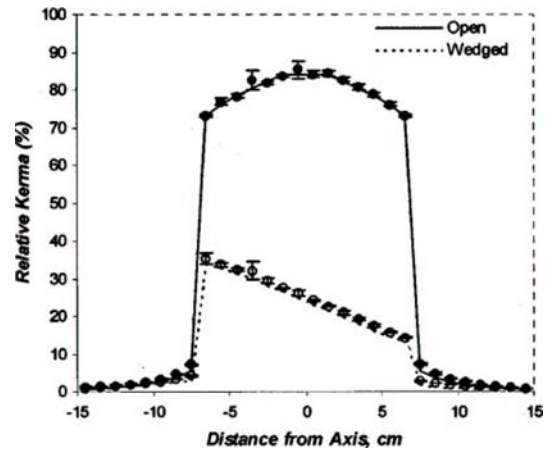


Fig. 4. Deterministic vs MC kerma transverse profiles at 4.5 cm depth for reference source.

The TransMED-LSU transport calculation computes kerma values at more than 13,000 locations for each run. These calculations used 20-28 energy groups, depending on the source spectra. The direction mesh consisted of 82 directions (including two directions along the positive and negative vertical axis), and the phantom was represented by 13,500 ($=30 \times 30 \times 15$) rectangular bodies, each with a 1 cm^3 volume. In all cases the deterministic and Monte Carlo calculations used identical 3D geometries and source distributions, so that differences in results can be attributed to differences in methodology and, to a lesser extent, in nuclear data. The MCNP input was generated by the TransMED code, which includes an option for this procedure in order to facilitate comparisons.

Figure 3 compares the central-axis kerma depth-dose profiles computed by TransMED-LSU and MCNP, for the four source spectra in Figure 2. Each curve is normalized to the maximum kerma value, K_{max} , for the reference case to give a relative percentage value. In all cases the deterministic kerma depth-dose profiles are essentially within the MCNP statistical margin, the differences being under 2%. It should be noted that Fig. 3 represents a completely independent and absolute comparison of the Monte Carlo and deterministic values; i.e., there has been no cross-normalization done. The consistency of the results for the different sources verifies that the deterministic formalism correctly models the physical processes for a variety of energy spectra.

Figure 4 shows the transverse kerma distributions calculated for the reference case (10MV/5mm-W source) at a depth of 4.5 cm from the phantom surface, both for an open field and with a wedge attenuator present. The open field profile computed by TransMED-LSU in the beam region agrees with the MCNP values within 2%, which is approximately the statistical uncertainty in the Monte Carlo results. In the umbra region of the profile, the discrepancy between MCNP and TransMED-LSU results becomes significant, often exceeding 15%; but the relative importance of these regions is usually not significant when multiple beams are used. The excellent agreement in the beam region for this case means that scattering from LINAC head components such as the flattening filter (which was estimated to contribute about 5% of the total kerma for this case) as well as the internal scattering by the phantom itself are correctly treated in TransMED-LSU.

To investigate the accuracy of the kerma predicted by the deterministic method when beam modifiers are present, an 8.5 degree wedge was added to the geometry, as shown in Fig. 1. The discrepancies between the TransMED and MCNP transverse profiles for the wedge case in Fig. 4 are slightly higher in the beam region than observed for the open field case. TransMED underestimates the kerma compared to MCNP results by about 2% at the peak, and 5-6% in the low dose region within the beam. In the umbra region outside the beam, the differences were up to 35%. Much of this observed systematic discrepancy is probably caused by second order scatter from the wedge. At this time the deterministic calculation does not take into account those photons that suffer a first collision in the flattening filter and subsequently a second (or higher order) scatter in the wedge, prior to reaching the phantom. Hence, an analytical second-collision source calculation should be added for beam-modifier components such as wedges and multileaf collimators, in the same manner that it is currently implemented for the patient/phantom region. We believe that by adding this contribution, differences between TransMED and MCNP can be reduced to an acceptable level.

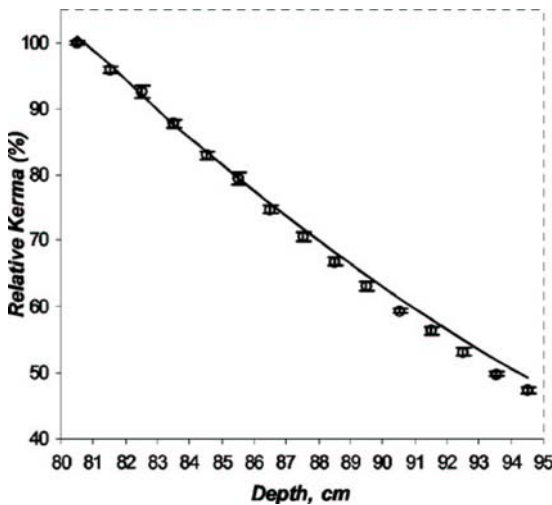


Fig. 5. Deterministic vs MC kerma depth dose profile for a 6 x 6 cm field.

Figure 5 shows the kerma percent depth-dose profiles for a 6x6 open field. The deterministic values for voxels in the beam generally agree within about 4% of the Monte Carlo results. There is a tendency for the deterministic calculation to overestimate kerma values (compared to Monte Carlo) at greater depths from the surface. This appears to be caused by the discrete angle treatment of the collision sources, as particles scattering in forward directions are assigned mostly to the quadrature direction lying directly along the vertical axis. This tends to increase the photon penetration at greater depths. A forward biased directional quadrature would improve the behavior, but this capability is not currently in TransMED.

The execution time required to obtain dose distribution for therapy planning is an important factor in clinical implementation. A crude comparison of the two approaches can be obtained by examining central processor unit (CPU) times to compute a consistent set of kerma responses, using the same computer platform for both methods. For the reference example case, TransMED took about 400 CPU minutes on a dual processor SUN Blade 1000 workstation to compute the kerma distribution for 13,500 bodies corresponding to a 1 cm³ spatial mesh in the phantom. For the same set of voxels, MCNP required about 650 CPU minutes to obtain kerma tallies with a tracklength estimator using 100 million histories. The MCNP statistical uncertainty for this case was around 1% in the beam region and 10% - 15% outside. The above one-sigma statistical errors have only a 68% confidence limit; therefore, if more meaningful Monte Carlo results are desired in the umbra region, the number of histories – and hence the execution time – should be significantly increased.

At this time, the computation algorithms in TransMED have not been optimized. The current code allows only a uniform (equal weights) set of quadrature directions. Because Compton scattering is generally forward peaked, a non-uniform distribution of directions biased along the vertical axis would treat photon scattering more efficiently. Similarly the number of

energy groups can be adjusted for speed and precision optimization. A significant improvement in execution time also could be achieved by optimizing the current ray tracing algorithm in TransMED, and taking advantage of the regular rectangular voxel geometry in the phantom.

CONCLUSIONS

The deterministic methodology currently implemented in TransMED has similar geometrical capabilities as typical Monte Carlo codes, and can represent LINAC head components and rectangular voxels corresponding to a phantom or patient image file with little approximation. Deterministic solution of the Boltzmann equation can theoretically provide as rigorous a calculation as Monte Carlo for determining dose distributions. Among potential advantages of a deterministic approach is the greater computational efficiency for obtaining higher resolution dose distributions; i.e., less execution time per dose point.

Deterministic transport calculations performed with the TransMED code predict the open field kerma distributions within ~ 2% of Monte Carlo results, for a water phantom exposed to a variety of LINAC photon beams. Kerma depth-dose and transverse distributions are predicted well. Agreement between deterministic and MC results for an wedged field was 2-6%, suggesting that additional refinements for treating higher order scatter from beam-modifier components may be required for some realistic treatment cases. This can be easily done by extending the present methodology in the TransMED code. The small kerma values for the umbra region outside of the field differ by 10-20% from the MCNP values, but the Monte Carlo results have relatively higher statistical uncertainties in this region.

The TransMED deterministic calculations are presently limited to computations of kerma, rather than absorbed dose. In regions where electronic disequilibrium is significant corrections for electron transport must be incorporated into the deterministic methodology. Hence, the dose in the initial buildup region at the surface and at interfaces of dissimilar media (e.g., tissue/lung) cannot be accurately calculated with currently available 3D deterministic codes. However, deterministic techniques have been developed for treating electron transport in one dimensional geometries⁽¹⁶⁾, and in theory these could be modified for implementation into a 3D general geometry deterministic code such as TransMED.

Although this stage of the TransMED code development is still incipient, we believe that further optimization of the geometry and ray tracing routines, parametric studies aimed at optimizing energy, angular, and spatial meshing, and more efficient memory management and input/output operations could decisively enhance the ability of deterministic transport methods to compete successfully with Monte Carlo based systems as a rigorous tool for photon transport calculations in external beam therapy applications. However development of new 3D deterministic techniques to account for electron transport will be necessary for practical implementation of the methodology to determine absorbed dose distributions.

REFERENCES

1. Ma CM, et al., "Clinical implementation of a Monte Carlo treatment planning system," *Med. Phys.* 26(10), 2133-2143 (1999)
2. DeMarco, Solberg TD, Smathers JB, "A CT-based Monte Carlo Simulation Tool for Dosimetry Planning and Analysis." *Med. Phys.* 25, 1-11 (1999)

3. E. E. Lewis and W. F. Miller, *Computational Methods of Neutron Transport*, (John Wiley and Sons, New York, 1984)
4. T. Postma and J. Vujic, "The method of characteristics in general geometry with anisotropic scattering," Proc. of the International Conference on Mathematics and Computation, Reactor Physics and Environmental Analysis in Nuclear Applications, Madrid, Spain, Vol.2, p.1215-1234 (1999)
5. S. G. Hong, N. Z. Cho, "CRX: A code for rectangular and hexagonal lattices based on the method of characteristics," *Ann. Nucl. Energy* 25, 545 (1998)
6. "TransMED medical physics software, user's manual," TransWare Enterprises, Inc., San Jose, CA, (Oct. 2000)
7. "TransFX: A modular software system for evaluating particle transport effects," TransWare Enterprises, Inc., San Jose, CA, (Oct. 2000)
8. Williams ML, Sajo E., "Deterministic Calculations of Photon Spectra for Clinical Accelerator Targets," *Med. Phys.* 29 (6): 1019-1028 (2002).
9. Lorence LJ, Morel JE, Valdez GD. "Physics Guide to CEPXS: A multigroup coupled electron-photon cross section generating code." SAND89-1685, Sandia National Laboratory, October, 1989.
10. O'Dell RD. "Revised Manual for ONEDANT: A code package for one-dimensional diffusion-accelerated neutral particle transport." LA-9184-M, Rev. December, 1989.
11. Williams ML et al. "Deterministic Photon Transport Calculations in General Geometry for External Beam Radiation Therapy." *Med Phys* 30 (12) 3183-3195 (2003).
12. J. F. Briesmeister, ed., "MCNP—A general Monte Carlo N-particle transport code/Version 4C," LA-13709-M, Los Alamos National laboratory (April 2000)

INTRODUCTION TO A³MCNP – AUTOMATED ADJOINT ACCELERATED MCNP

A. Haghghat
Department of Nuclear and Radiological Engineering
University of Florida

One of the difficulties with the MC method is the need for large computational time, which requires the use of variance reduction (VR) techniques. The VR techniques, however, are diverse and generally require determination of problem-dependent parameters which are difficult to estimate. Incorrect use of VR techniques, either because of the use of inappropriate technique(s) or parameters, may lead to “biased” results that, depending on the user's experience, may or may not be apparent to the user.

To overcome this difficulty, the A³MCNP - Automatic Adjoint Accelerated MCNP code system was developed.[1-3] A³MCNP is a revised version of the widely-used, general-purpose MCNP code [4] that has been modified to automatically prepare variance reduction parameters for the CADIS (Consistent Adjoint Driven Importance Sampling) variance reduction methodology developed for fixed source problems.[1-3] CADIS, performs source biasing and consistent transport biasing within the weight-window technique. CADIS uses the adjoint function distribution obtained from deterministic Sn transport calculations to prepare biased source, and lower weight of the weight-window technique. To determine the adjoint function distribution, A³MCNP prepares the necessary input files for performing multigroup, three-dimensional adjoint Sn transport calculations using TORT [5]. For this task, A³MCNP prepares a mesh distribution and the corresponding mixtures and their identification numbers and densities. Necessary data on geometry and material are mainly extracted from the standard MCNP input; therefore, requiring only five additional input cards. A³MCNP performs following tasks:

- 1) Prepares the necessary input files for a deterministic adjoint calculation
 - Generation of a mesh distribution for a deterministic adjoint calculation. Mesh generator utility first generates a uniform mesh distribution to extract information on material distribution, and then through a back-thinning process prepares a variable mesh distribution.
 - Preparation of input file for the TORT Sn code.
 - Determination of material compositions and preparation of input files for the GIP code [5] for generation of multigroup cross sections.
- 2) Reads the adjoint (importance) function from the standard TORT binary output file and prepares source biasing parameters and space- and energy-dependent weight window lower bounds.
- 3) Superimposes the detailed weight window values (based on the deterministic spatial-mesh distribution and energy-group structure) onto the Monte Carlo model and uses them in a transparent manner.

A³MCNP has been used for the simulation of a few real-life problems, including a PWR pressure vessel and cavity dosimeter [6], a BWR core shroud [7], and spent fuel shipping and storage casks [8 and 9].

Cavity dosimetry calculations [6] attempt to estimate reaction rates in a small volume outside of the Reactor Pressure Vessel (RPV) at a distance of ~350 cm from the core centerline. These reaction rates are used to validate methods/models that are subsequently used to estimate the RPV neutron fluence.

Without the use of variance reduction techniques, one could allow MCNP to run this problem continuously for weeks and still not obtain statistically significant/reliable results [6]. Before the CADIS methodology and the A³MCNP code were developed, this problem was manually optimized [10] with existing variance reduction methods, including source biasing, weight windows, exponential transformation, implicit capture, and energy cutoff. This manual optimization required a great deal of time and effort to develop, but proved to be successful in terms of both computational performance and calculational reliability (i.e., enabled problem objectives to be accomplished with available computational resources). During the development of the automated variance reduction methodology, the problem was used to evaluate the efficiency of the automated variance reduction approach (1,6). Initial application of the CADIS methodology, which was based on a 2-D adjoint function, increased the calculational efficiency by a factor of 4 with respect to our best manually optimized model and by a factor of ~50,000 with respect to the unbiased case. Furthermore, the automated variance reduction approach required very little user time, effort, or experience.

In Reference 7, we present application of A³MCNP to simulation of a BWR core shroud for determination of DPA at weld locations in a core shroud. In this study, we examined the impact of the degree of accuracy of deterministic adjoint. The study demonstrated that all cases tested resulted in significant speedups over the unbiased Monte Carlo. A maximum speedup of over 2000 was achieved.

In Refs. 8 and 9, we present use of A³MCNP for determination of neutron and gamma dose on the surface of a storage cask. A³MCNP, after 200 min (including 20 min for TORT), yields a relative error of 7.2%, while the unbiased case after 6000 min yield a relative error of 83%; this indicates that the unbiased MCNP requires at least ~569 CPU-days (1.6 years) in order to reduce the error to ~7%. Note that to obtain the dose on the top or bottom of the cask, the unbiased MCNP requires years of calculations!

In summary, A³MCNP is an effective tool for performing Monte Carlo simulations for large real-world problems.

1. J.C. Wagner, "Acceleration of Monte Carlo Shielding Calculations with an Automated Variance Reduction Technique and Parallel Processing," Ph.D. Thesis, The Pennsylvania State University, Nuclear Engineering Dept. (1997).
2. J.C. Wagner and A. Haghghat, "Automated Variance Reduction of Monte Carlo Shielding Calculations Using the Discrete Ordinates Adjoint Function," Nuclear Science and Engineering, 128, 186 (1998).
3. Haghghat, A. and J.C. Wagner, "Monte Carlo Variance Reduction with Deterministic Importance Functions," Progress of Nuclear Energy Journal, Vol. 42 (1), Jan. 2003.
4. J.F. Briesmeister, Editor, MCNP "A General Monte Carlo N-Particle Transport Code, Version 4A," LA-12625, Los Alamos National Laboratory (1993).

5. W.A. Rhoades and R.L. Childs, "TORT - Two- and Three-Dimensional Discrete Ordinates Transport, Version 1.515," CCC-543, ORNL-RSICC, Oak Ridge, TN, 1992.
6. J.C. Wagner and A. Haghight, "Acceleration of Monte Carlo Reactor Cavity Dosimetry Calculations with the Discrete Ordinates Adjoint Function," Proceedings of the 9th International Symposium on Reactor Dosimetry, edited by H. Abderrahim and H. Nolthenius, World Scientific Publishing Co., 1998.
7. A. Haghight, H. Hiruta, B. Petrovic, and J.C. Wagner, "Performance of the Automated Adjoint Accelerated MCNP (A³MCNP) for Simulation of a BWR Core Shroud Problem," Proceedings of the International Conference on Mathematics and Computation, Reactor Physics, and Environmental Analysis in Nuclear Applications, Madrid, Spain, September 27-30, 1999.
8. Haghight, A. and J. C. Wagner, "Application of A³MCNP to Radiation Shielding Problems," Advanced Monte Carlo for Radiation Physics, Particle Transport Simulation and Applications, pp. 619-624, Springer-Verlag, 2001.
9. Shedlock D. and A. Haghight, "Neutron analysis of spent fuel storage installation using parallel computing and advance discrete ordinates and Monte Carlo techniques," Journal of Radiation Protection Dosimetry, 116(1-4):662-666, Oxford University Press, Dec. 2005.
10. Wagner, J. C., A. Haghight, and B. G. Petrovic, "Monte Carlo Transport Calculations and Analysis for Reactor Pressure Vessel Neutron Fluence," Nuclear Technology, June 1996.

A REVISED STYLIZED PHANTOM AND VOXELIZED MODEL OF THE EXTRATHORACIC AND THORACIC REGIONS FOR USE IN NUCLEAR MEDICINE INTERNAL DOSIMETRY

Eduardo B. Farfán
Idaho State University

In this study, two different models are presented. The first model, a stylized (mathematical) phantom, was revised to generate tables of absorbed fractions for a large number of photon emitters (1). These tables were then used to determine doses to various thoracic, extrathoracic, and abdomen organs and tissues from inhalation of these photon emitters using a computer code based on International Commission on Radiological Protection (ICRP) Publication 66 (2). The second model, a voxelized model, was created to estimate lung burdens from the inhalation of plutonium dioxide aerosols at nuclear weapons facilities. Monte Carlo methods, MCNP, were utilized to develop both models. With minimal modifications, if any, these very distinct models could be used in nuclear medicine internal dosimetry to obtain comprehensive data of absorbed fractions and S values for various radiopharmaceuticals.

The first model shown in Figure 1 addresses the thoracic and extrathoracic (head) regions. The extrathoracic airways and lymph nodes have not yet been represented explicitly in ICRP (or MIRD) mathematical or stylized models of the human body when considering the transport of photons internally between source and target organs. Currently, the ICRP assumes that the extrathoracic airways are reasonably approximated by using the thyroid or brain as the surrogate source and target region within the ICRP 66 respiratory tract model. A new mathematical model was created to explicitly consider the extrathoracic airways, as well as other respiratory structures in the thorax of the adult. The model merges the revised MIRD model of the adult head and brain (3-4) with the ORNL model of the adult male torso and legs (5). Several modifications are made to include a number of organs and tissue regions absent in previous models. The revised model includes an external nose, nasal cavity, nasal sinuses (frontal, ethmoid, sphenoid, and maxillary), oral cavity, larynx, pharynx, trachea, and the extrapulmonary main bronchi. The thyroid is also modified to accommodate the new model of the larynx. In addition, sublayers of the external nose and of the larynx/pharynx are explicitly delineated to represent the target tissues of ET1 and ET2 as anatomically defined in ICRP Publication 66. The revised ET1 and ET2 regions are implemented within the MCNP radiation transport code to determine values of specific absorbed fraction (SAF) for monoenergetic photons for some 34 tissues and organs. These specific absorbed fractions are currently applied to an interactive computer program, LUDUC (Lung Dose Uncertainty Code) to estimate uncertainties in human respiratory tract (HRT) doses following inhalation of photon emitters selected from a list of some 233 radionuclides (6-12). Additional defining equations are established for the external nose, nasal cavity, nasal sinuses (frontal, ethmoid, sphenoid, and maxillary sinuses), oral cavity, larynx, pharynx, trachea, and main bronchi.

The second model, shown in Figures 2 and 3, used CT data of an entire human body to represent the body as a voxelized model in MCNP. The voxels have dimensions of 2 mm. In this model, the various organs and tissues of the thoracic and extrathoracic regions are included. The model also considers the extremities and abdomen organs and tissues. The organs and tissues are well-defined in this model.

The original uses of these models were the estimation of doses to various regions of the respiratory tract from the inhalation of PuO_2 particles produced during nuclear weapons production. The revised stylized model presented here provides an important improvement in the anatomic modeling of the extrathoracic region and the voxelized model presented a much more detailed representation of the human body. Both models could easily be applied in nuclear medicine internal dosimetry to determine AF and S values for a variety of radiopharmaceuticals. In these models, the radiation source (or sources) can be located in any region (organ or tissues) within the body or can be externally located.

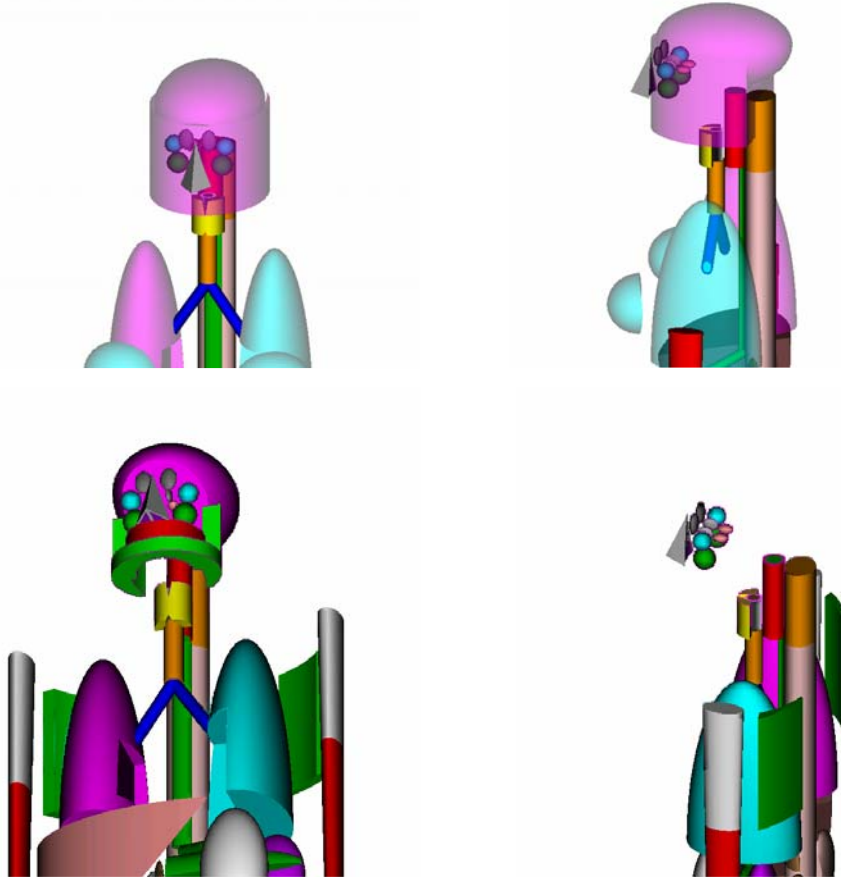


Figure 1. Views of the revised mathematical model of the adult.

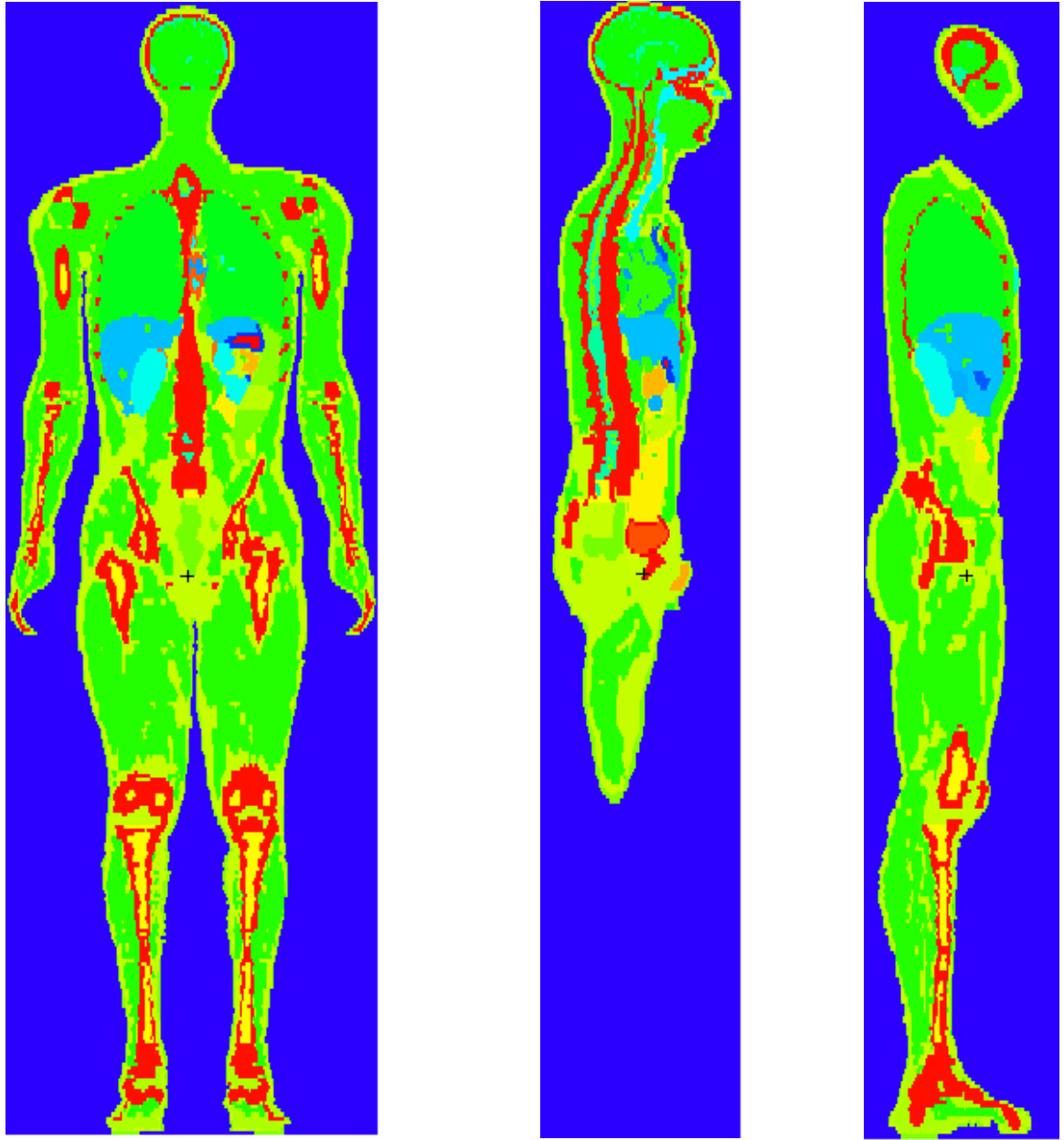


Figure 2. Views of the model based on CT data.

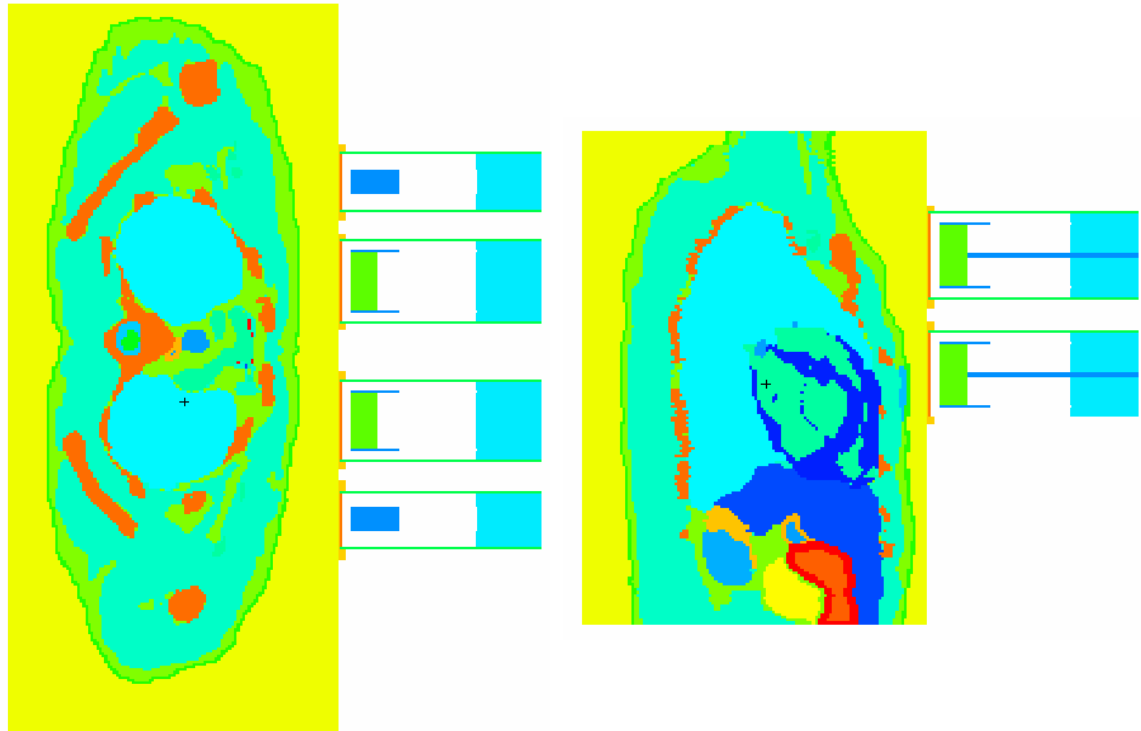


Figure 3. Views of the second model with detectors.

References

1. Farfán, EB; Han, EY; Bolch, WE; Huh, C; Huston, TE; Bolch, WE. A revised stylized model of the adult extrathoracic and thoracic airways for use with the ICRP-66 respiratory tract model. *Health Phys* 86(4):337-352; 2004.
2. ICRP. Human respiratory tract model for radiological protection. Oxford; Pergamon Press: International Commission on Radiological Protection. ICRP Publication 66; 1994.
3. Bouchet LG, Bolch WE, Weber DA, Atkins HL, Poston JW, Sr. MIRDPamphlet No. 15: Radionuclide S values in a revised dosimetric model of the adult head and brain. *Medical Internal Radiation Dose. J Nucl Med* 40:62S–101S; 1999.
4. Bouchet LG, Bolch WE, Weber DA, Atkins HL, Poston JW. A revised dosimetric model of the adult head and brain. *J Nucl Med* 37:1226–1236; 1996.
5. Eckerman KF, Westfall RJ, Ryman JC, Cristy M. Availability of nuclear decay data in electronic form, including beta spectra not previously published. *Health Phys* 67:338-345.; 1994.
6. Bolch WE, Farfán EB, Huh CH, Huston TE, Bolch WE. Influences of parameter uncertainties within the ICRP-66 respiratory tract model: Particle deposition. *Health Phys.* 81:378-394; 2001.
7. Bolch WE, Huston TE, Farfán EB, Vernetson WG, Bolch WE. Influences in parameter uncertainties within the ICRP-66 respiratory tract model: Particle clearance. *Health Phys* 84:421-435; 2003.
8. Farfán, E. B. Probabilistic Lung Dosimetry with Application to Uranium Dioxide and Uranium Octoxide Aerosols [Thesis]. Gainesville, Florida: University of Florida. 1999. [Available from UF, 202 NSB, P.O. Box 118300 (Phone No. 1-352-392-1401)].

9. Farfán, E. B. Probabilistic Respiratory Tract Dosimetry Model with Application to Beta-Particle and Photon Emitters [Dissertation]. Gainesville, Florida: University of Florida. 2002. [Available from UF, 202 NSB, P.O. Box 118300 (Phone No. 1-352-392-1401)].
10. Farfán EB, Huston TE, Bolch WE, Vernetson WG, Bolch WE. Influences of parameter uncertainties within the ICRP-66 respiratory tract model: Regional tissue doses for $^{239}\text{PuO}_2$ and $^{238}\text{UO}_2/^{238}\text{U}_3\text{O}_8$. Health Phys 84:436-450; 2003.
11. Huston TE. Quantifying Uncertainties in Lung Dosimetry with Application to Plutonium Oxide Aerosols [Dissertation]. Gainesville, Florida: University of Florida. 430; 1995.
12. Huston TE, Farfán EB, Bolch WE, Bolch WE. Influences of parameter uncertainties within the ICRP-66 respiratory tract model: A parameter sensitivity analysis. Health Phys 84:553-566; 2003.

INTERNAL DISTRIBUTION

- | | | | |
|-----|------------------|-----|-----------------|
| 1. | Hatice Akkurt | 11. | Saed Mirzadeh |
| 2. | Dana Christensen | 12. | Cecil Parks |
| 3. | Kevin Clarno | 13. | Douglas Peplow |
| 4. | Michael Dunn | 14. | A. F. Rice |
| 5. | Dan Ilas | 15. | Jim Rushton |
| 6. | Germina Ilas | 16. | John Wagner |
| 7. | Bernadette Kirk | 17. | Mark Williams |
| 8. | Luiz Leal | 18. | Brain Worley |
| 9. | Dick Lillie | 19. | Thomas Zacharia |
| 10. | Reinhold Mann | | |

EXTERNAL DISTRIBUTION

20. Cassiano De Oliveira, Georgia Institute of Technology, Nuclear and Radiological & Medical Physics Program, GWW School of Mechanical Engineering, Atlanta, GA 30332-0405
21. James A. Deye, National Cancer Institute, MSC 7440, 6130 Executive Blvd., Rockville, MD 20892-7440
22. Eduardo Farfan, Idaho State University, 785 S. 8th Ave., Campus Box 8106, Pocatello, ID 83209
23. Tim Goorley, Los Alamos National Laboratory, Code Development, X-3, MS F663, Los Alamos, NM 87545
24. Ali Haghghat, University of Florida, PO Box 118300, Gainesville, FL 32611-8300
25. Robert Jeraj, University of Wisconsin - Madison, 1530 Medical Sciences Center, 1300 University Ave, Madison, WI 53706
26. Harriet Karagiannis, U.S. Nuclear Regulatory Commission, 9 C34, 11545 Rockville Pike, Rockville, MD 20852-2738
27. Michael E. Kowalok, Virginia Commonwealth University, Radiation Oncology, Box 980058, 401 College St / North Hosp., Richmond, VA 23284
28. Wayne Newhauser, The University of Texas M. D. Anderson Cancer Center, 1515 Holcombe Blvd, Houston, TX 77030
29. Trent Nichols, The Univ. of Tennessee Medical Center, Department of Radiology, 1924 Alcoa Highway, Knoxville, TN 37920
30. Dave Nigg, Idaho National Laboratory, MS 3860, PO Box 1625, Idaho Falls, ID 83415
31. Farzad Rahnema, Georgia Tech, School of Mech. Engg., MS 0405, Atlanta, GA 30332-0405
32. Mark Rivard, Tufts University, New England Medical Center, Dept. of Rad. Onc. Box 246, 750 Washington Street, Boston, MA 02111
33. Erno Sajo, Louisiana State University, Nuclear Science Center, Baton Rouge, LA 70803-5820
34. Megan Satterfield, Georgia Tech, Atlanta, GA 30332-0405
35. Sam Sherbini, U.S. Nuclear Regulatory Commission, MS T8F5, 11545 Rockville Pike, Rockville, MD 20852
36. Glenn Sjoden, University of Florida, 202 Nuclear Science Bldg., Gainesville, FL 32606
37. Benny Titz, University of Wisconsin, Department of Medical Physics, 1530 Medical Sciences Center, 1300 University Ave, Madison, WI 53706
38. Dingkang Zhang, Georgia Tech, Atlanta, GA 30332-0405